



HAL
open science

Middle Devonian, late Carboniferous, and Triassic magmatic flare-ups in eastern Armorica (Sakarya Zone, Turkey) as revealed by detrital zircon U-Pb-Hf isotopic data

Gültekin Topuz, Osman Candan, Oscar Laurent, Ali Mohammadi, Cengiz Okuyucu, Ömer Faruk Çelik, Jia-Min Wang

► To cite this version:

Gültekin Topuz, Osman Candan, Oscar Laurent, Ali Mohammadi, Cengiz Okuyucu, et al.. Middle Devonian, late Carboniferous, and Triassic magmatic flare-ups in eastern Armorica (Sakarya Zone, Turkey) as revealed by detrital zircon U-Pb-Hf isotopic data. *Geological Society of America Bulletin*, 2023, 136 (7-8), pp.3053-3068. 10.1130/B36950.1 . hal-04793406

HAL Id: hal-04793406

<https://hal.science/hal-04793406v1>

Submitted on 21 Nov 2024

HAL is a multi-disciplinary open access archive for the deposit and dissemination of scientific research documents, whether they are published or not. The documents may come from teaching and research institutions in France or abroad, or from public or private research centers.

L'archive ouverte pluridisciplinaire **HAL**, est destinée au dépôt et à la diffusion de documents scientifiques de niveau recherche, publiés ou non, émanant des établissements d'enseignement et de recherche français ou étrangers, des laboratoires publics ou privés.

1 **Middle Devonian, Late Carboniferous and Triassic magmatic flare-ups in the**
2 **Eastern Armorica (Sakarya Zone, Turkey) as revealed by detrital zircon U-**
3 **Pb-Hf isotopic data**

4
5 Gültekin Topuz^{1,*}, Osman Candan², Oscar Laurent^{3,4}, Ali Mohammadi¹, Cengiz Okuyucu⁵,
6 Ömer Faruk Çelik⁶, Jia-Min Wang⁷

7
8 ¹ *İstanbul Teknik Üniversitesi, Avrasya Yer Bilimleri Enstitüsü, TR34469 Maslak, İstanbul,*
9 *Turkey; E-mail: topuzg@itu.edu.tr (<https://orcid.org/0000-0001-8690-4614>);*
10 *mohammadiali@itu.edu.tr*

11 ² *Dokuz Eylül Üniversitesi, Jeoloji Mühendisliği Bölümü, Tınaztepe Yerleşkesi, Buca, İzmir,*
12 *Turkey; E-mail: osman.candan@deu.edu.tr*

13 ³ *ETH Zurich, Department of Earth Sciences, Institute for Geochemistry and Petrology,*
14 *Clausiusstrasse 25, 8092, Zurich, Switzerland*

15 ⁴ *CNRS, Géosciences Environnement Toulouse, Observatoire Midi-Pyrénées, 14 avenue Edouard*
16 *Belin F-31400 Toulouse, France. E-mail: oscar.laurent@get.omp.eu*

17 ⁵ *Konya Teknik Üniversitesi, Jeoloji Mühendisliği Bölümü, 42250 Selçuklu, Konya, Turkey. E-*
18 *mail: cokuyucu@ktun.edu.tr*

19 ⁶ *Kocaeli Üniversitesi, Jeoloji Mühendisliği Bölümü, Umuttepe Yerleşkesi, TR41001 Kocaeli,*
20 *Turkey; E-mail: celikfrk@gmail.com*

21 ⁷ *State Key Laboratory of Lithospheric Evolution, Institute of Geology and Geophysics, Chinese*
22 *Academy of Sciences, 19 Beitucheng West Road, Chaoyang District, 100029 Beijing, China, E-*
23 *mail: wangjm9595@gmail.com*

24 **ABSTRACT**

25 The Sakarya Zone (northern Turkey) contains a well-preserved Early-Middle Jurassic and Late
26 Cretaceous submarine magmatic arc constructed over pre-Jurassic bedrocks that are considered to
27 be the eastward extension of the Armorican Terrane Assemblage in Europe. In this study, we
28 present U-Pb-Hf isotopic data on the detrital zircons from Middle Permian and Lower Jurassic
29 sandstones to reveal episodes of Paleozoic–Early Mesozoic magmatic flare-ups. Detrital zircon
30 ages together with data from the literature define three major age groups at 400–380, 326–310
31 and 250–230 Ma, indicating three distinct magmatic flare-ups. In addition, there are minor age
32 clusters at 460–430 and 215–195 Ma. Initial ϵ_{Hf} values of the detrital zircons indicate a
33 significant juvenile input during the Triassic flare-up, the involvement of significant reworked
34 crustal material during the Late Carboniferous magmatic flare-up, and both juvenile and
35 reworked crustal material during the Middle Devonian magmatic flare-up. Within the pre-
36 Jurassic continental basement rocks of the Sakarya Zone, the Late Carboniferous igneous rocks
37 are well documented and most voluminous, and the Middle Devonian rocks are known locally,
38 while the Triassic igneous rocks apart from those in Triassic accretionary complexes are hardly
39 known. Because the Sakarya Zone is a Gondwana-derived continental block that was later
40 involved in the Variscan and Alpine orogenies, these magmatic flare-ups cannot be explained by
41 subduction-related processes along a single subduction zone. We propose that the Sakarya Zone
42 rifted from the northern margin of Gondwana during Late Ordovician-Silurian, the Devonian
43 magmatic flare-up (400–380 Ma) was related to the southward subduction of the Rheic ocean
44 beneath the Sakarya Zone during its northward drift and the Late Carboniferous magmatic flare-
45 up (326–310) occurred following the collision of the Sakarya Zone with Laurussia, and the
46 Triassic one (250–230 Ma) resulted from northward subduction of the Tethys ocean beneath the

47 Sakarya Zone. Comparison with literature data shows that the Triassic and Late Carboniferous
48 magmatic flare-ups are also characteristic features of neighboring Armorican domains such as the
49 Balkans and the Caucasus; however, the Middle Devonian flare-up appears to be restricted to the
50 Sakarya Zone. Along with the Late Carboniferous flare-up, the Late Ordovician-Silurian flare-up
51 which is locally recorded in the Sakarya Zone is typical of the Armorican Terrane Assemblage as
52 a whole.

53 **Key-Words:** Sandstone, provenance, U-Pb zircon age, zircon Hf isotopy, magmatic flare-up,
54 Sakarya Zone, Armorica, Turkey

55

56 INTRODUCTION

57 In orogenic belts, the intensity of magmatic activity shows temporal and spatial
58 variations. In general, episodes of high-volume magmatism alternate with those of low-volume or
59 no magmatism (e.g., DeCelles et al., 2009; Kirsch et al., 2016; Paterson and Ducea, 2015; Zhang
60 et al., 2020; Chapman et al., 2021). Episodes of high-volume magmatism are referred to as
61 magmatic flare-ups and episodes of low-volume magmatism as magmatic lulls. In general,
62 magmatic flare-ups last 5 to 20 Ma, while magmatic lulls occur over 30 to 70 Ma. Although it is
63 difficult to determine the exact volume of magma produced during flare-up events, estimated
64 production rates range from 140 to 215 km³/km·Ma during flare-ups, and less than 15
65 km³/km·Ma during lulls (Chapman et al., 2021). The proposed drivers for such magmatic flare-
66 up events are multiple, including (i) changes in convergence rate, (ii) slab roll-back, (iii) slab
67 breakoff, slab tear and lithospheric delamination, (iv) repeated magmatic underplating of the
68 lower crust, and (v) lithospheric thickening in the fore-arc and back-arc domains (e.g. Ducea and
69 Barton, 2007; Paterson and Ducea, 2015; Shellnutt et al., 2014; Ardila et al., 2019; Zhang et al.,
70 2019).

71 Episodes of the magmatic flare-ups and lulls are best constrained by combining the
72 relative abundance of detrital zircon ages from clastic sedimentary rocks with the ages of exposed
73 igneous rocks and their estimated volumes (e.g. Paterson and Ducea, 2015; Zhang et al., 2019;
74 Chapman et al., 2021). In several orogenic belts such as the Sierra Nevada arc in California and
75 the Neo-Tethyan arc system in south Asia (Paterson and Ducea, 2015; Zhang et al., 2019;
76 Balgord et al., 2021), detrital zircon age clusters match well the timing of high-volume
77 magmatism, except for the case of dominant basic magmatism. Although clusters of the detrital
78 zircon ages are affected by various factors such as sampling bias and relative abundance of
79 zircons in different rock types (e.g. Moecher and Samson, 2006; Dickinson, 2008; Malusa et al.,
80 2013; Anderson et al., 2019), in ancient and/or long-lived orogenic belts, detrital zircon ages are
81 the primary means of revealing magmatic flare-ups (e.g., Balgord et al., 2021; Pastor-Galan et al.,
82 2021), as the igneous rocks related to former flare-ups may be largely eroded, metamorphosed, or
83 buried under younger volcanic-sedimentary strata.

84 The Sakarya Zone (northern Turkey) contains a well-preserved Early-Middle Jurassic and
85 Late Cretaceous submarine magmatic arc that was constructed over pre-Jurassic bedrock mostly
86 buried under Jurassic and younger volcanic-sedimentary strata (Figs. 1 and 2) (Şen, 2007; Okay
87 and Nikishin, 2015). Pre-Jurassic basement outcrops account for only about 10% of the total
88 outcrops and probably represent the eastern extension of the Armorican Terrane Assemblage in
89 central Europe (e.g. Winchester and the Pace TMR Network Team, 2002; Okay et al., 2006;
90 Okay and Topuz, 2017). The Armorican Terrane Assemblage or simply Armorica *sensu* Franke
91 includes Armorican Massif, Vosges, Black Forest and Bohemian Massif. In this study, we present
92 U-Pb-Hf isotope data on detrital zircons from Middle Permian sandstones in a Permo-Triassic
93 accretionary complex and from Lower Jurassic sandstones unconformably overlying the pre-
94 Jurassic basement to reveal the pre-Jurassic magmatic flare-ups. The U-Pb zircon age clusters

95 together with literature data define three major flare-up events at 400–380 (latest Early to earliest
96 Late Devonian), 326–310 (latest Early to Late Carboniferous) and 250–230 Ma (Early to earliest
97 Late Triassic; after Cohen et al. 2013 updated). For the sake of brevity, the flare-ups at 400–380,
98 326–310 and 250–230 Ma are hereinafter referred to as Middle Devonian, Late Carboniferous
99 and Triassic, respectively. Furthermore, we present an evolutionary model for the Paleozoic and
100 early Mesozoic evolution of the Sakarya Zone beginning with the rifting from the northern
101 margin of Gondwana during Late Ordovician-Silurian, continuing with northward drift and
102 accretion into Laurussia during the Early Carboniferous and ending with the Permo-Triassic
103 subduction of the Paleo-Tethys beneath the Laurasia.

104

105 **GEOLOGICAL FRAMEWORK**

106 The Sakarya Zone (northern Turkey) is a Gondwana-derived continental fragment bound
107 by the Intra-Pontide suture and the Black Sea to the north and the Izmir-Ankara-Erzincan suture
108 to the south (Fig. 2). Its pre-Jurassic bedrock can be divided into two parts: (i) a continental
109 domain mainly of Carboniferous to Middle Permian age, and (ii) Permo-Triassic sedimentary and
110 low-grade metamorphic rocks interpreted as accretionary complexes, commonly known as the
111 Karakaya Complex (Figs. 2 and 3). The continental domain consists of several units such as (i)
112 Early Carboniferous high-temperature / middle- to low-pressure (*HT-M* to *LP*) metamorphic
113 rocks intruded by various types of Early Carboniferous to Early Permian acidic to basic
114 intrusions (Nzegge et al., 2006; Topuz et al., 2004b, 2010, 2023; Dokuz, 2011; Kaygusuz et al.,
115 2012, 2016; Ustaömer et al., 2012, 2013; Karlı et al., 2016), (ii) Upper Carboniferous to Lower
116 Permian sedimentary rocks (Okay and Leven, 1996; Dokuz et al., 2017), and (iii) Early to Middle
117 Devonian non-metamorphic granites intruding undated low-grade metamorphic rocks (Okay et

118 al., 2006; Aysal et al., 2012; Sunal, 2012). The Early Carboniferous HT-M to LP metamorphic
119 units comprise metasedimentary rocks mainly of Late Neoproterozoic to Early Paleozoic
120 protolith ages and acidic to ultrabasic meta-igneous rocks with Ordovician to Early
121 Carboniferous igneous crystallization ages (e.g., Dokuz et al., 2022; Karşlı et al., 2020; Topuz et
122 al., 2020). The Permo-Triassic accretionary complexes include (i) greenschist to blueschist- and
123 epidote-amphibolite-facies metamorphic rock assemblages, consisting of metabasite, marble,
124 phyllite and minor metachert and serpentinite (the Lower Karakaya Complex), and (ii) non-
125 metamorphic to very low-grade sandstone, basalt and limestone (the Upper Karakaya Complex)
126 (Pickett and Robertson, 1996; Okay et al., 2002, 2020; Okay and Göncüoğlu, 2004; Topuz et al.,
127 2004a, 2014, 2018; Robertson and Ustaömer, 2012). Ar-Ar phengite dating on the Lower
128 Karakaya Complex gave metamorphic ages ranging from 262 to 195 Ma (Middle Permian to
129 earliest Jurassic) (Okay and Monié, 1997; Okay et al., 2002, 2020; Topuz et al., 2004a, 2014,
130 2017). The metaophiolite fragments record Early to Middle Permian igneous crystallization ages
131 (274–263 Ma) (Topuz et al., 2018; Okay et al., 2020). The metabasic and basaltic rocks in both
132 the Lower and Upper Karakaya complexes exhibit mainly anorogenic alkaline affinities similar to
133 those found in seamounts, suggesting seamount accretion during the Late Triassic (Pickett and
134 Robertson, 1996; Sayit and Göncüoğlu, 2009). In places, the Permo-Triassic accretionary
135 complexes are tectonically juxtaposed with the Early to Middle Jurassic accretionary complexes,
136 ophiolites and Late Cretaceous ophiolitic mélanges. This suggests a history of subduction and
137 accretion from Middle Permian to Late Cretaceous time.

138 All the pre-Jurassic basement units are overlain with a major unconformity by Early to
139 Late Jurassic sedimentary and volcanoclastic rocks and locally with Ammonitico Rosso limestone
140 horizons in the eastern to central part of the Sakarya Zone (Fig. 2; Altıner et al., 1991; Şen, 2007;

141 Kandemir and Yılmaz, 2009; Vincent et al., 2018). Exposures of the Jurassic volcanoclastic rocks
142 in the western part of the Sakarya Zone are minor (Genç and Tüysüz, 2010). The volcanoclastic
143 rocks formed in a time interval from the Pliensbachian to the latest Oxfordian-early
144 Kimmeridgian (183–158 Ma; Cohen et al. 2013 updated), and exhibit lateral facies and thickness
145 variations. These features led to the interpretation that they formed in a rifting environment (Şen,
146 2007, and the references therein). The volcanoclastic rocks pass up into neritic carbonates which
147 are Late Jurassic to Early Cretaceous in age (Altıner et al., 1991; Vincent et al., 2018). The basal
148 levels of the volcanoclastic sequence occupy a crucial position in determining the major pre-
149 Jurassic magmatic flare-ups, as they overlay various bedrocks with a major unconformity.

150 In clear contrast to the Sakarya Zone, the Anatolide-Tauride Block is characterized by
151 Paleozoic to Late Mesozoic sedimentary rocks (mainly carbonates) with local unconformities and
152 lacks any Early Carboniferous *HT-M* to *LP* metamorphism and deformation (e.g. Özgül and
153 Kozlu, 2002; Özgül, 1983; Robertson et al., 2021; Fig. S1). Paleozoic magmatism is minor and
154 local. Nevertheless, Triassic magmatism is more widespread. The Triassic unconformities in the
155 Anatolide-Tauride Block as well as the lateral facies and thickness changes in the Jurassic
156 volcanoclastic rocks of the Sakarya Zones have been attributed to a rifting event that resulted in
157 the opening of the Neo-Tethyan ocean (e.g. Şengör and Yılmaz, 1981; Şengör et al. 2019).
158 However, several lines of evidence such as (i) the presence of the Permo-Triassic, Jurassic, and
159 Late Cretaceous accretionary complexes in the Sakarya Zone, (ii) blocks or slivers of Permian
160 ophiolite as well as Middle Devonian, Carboniferous, Permian and Triassic cherts in the Permo-
161 Triassic accretionary complexes, and (iii) Middle Triassic to Upper Cretaceous radiolarites in the
162 Late Cretaceous accretionary complexes conclusively suggest that the Izmir-Ankara-Erzincan
163 suture represents the trace of a long-lived oceanic domain from at least Silurian to Late

164 Cretaceous (e.g. Pickett and Robertson, 1996; Tekin et al., 2002; Robertson and Ustaömer, 2012;
165 Okay et al. 2013, 2020; Topuz et al. 2013a, 2014, 2017).

166

167 **THE TOKAT MASSIF**

168 The Tokat Massif is a large metamorphic area (ca. 18 000 km²) to the southwest of the
169 Eastern Pontides, and consists of Permo-Triassic to Late Jurassic low-grade to non-metamorphic
170 rocks tectonically interleaved with several east-west trending sheets of Late Cretaceous ophiolitic
171 *mélange*, 0.2 to 2 km across and up to 60 km long (Figs. 2 and 4). The low-grade metamorphic
172 rocks comprise transitional greenschist- to blueschist-facies metabasite, marble, phyllite and
173 minor metachert and serpentinite (e.g., Rojay and Göncüoğlu, 1997; Yılmaz et al., 1997; Yılmaz
174 and Yılmaz, 2004; Eyüboğlu et al., 2011, 2018; Catlos et al., 2013, Topuz et al., 2022). Within
175 the metamorphic rocks, there are Triassic anorogenic tholeiitic to alkaline metagabbros as well as
176 Early Devonian and Permian limestone olistoliths in predominantly Triassic metaclastic rocks
177 (Çapkinoğlu and Bektaş, 1997; Eyüboğlu et al., 2018). The anorogenic tholeiitic to alkaline
178 metagabbros with igneous crystallization ages of 245–203 Ma are dominant meta-igneous
179 lithologies in the Tokat Massif (Eyüboğlu et al., 2011, 2018). On the other hand, the Late
180 Cretaceous ophiolitic *mélanges* comprise basalt, gabbro, radiolarite, serpentinite, sandstone,
181 shale, limestone, trondhjemite and metamorphic rocks (e.g., Bozkurt et al., 2007; Çelik et al.
182 2019a-b). The Tokat Massif is interpreted either as a Triassic marginal basin that developed on
183 the northern margin of Gondwana (Şengör and Yılmaz, 1981; Şengör et al., 2019; Eyüboğlu et al.
184 2018) or as a Permo-Triassic accretionary complex related northward subduction of Paleo-Tethys
185 beneath the Laurasia (Okay and Göncüoğlu, 2004; Topuz et al., 2014).

186

187 **THE MIDDLE PERMIAN AND LOWER JURASSIC SANDSTONES**

188 In the northern part of the Tokat Massif, there is a dismembered formation composed of
189 blocks/olistoliths of Lower to Middle Permian neritic limestone in a clastic matrix, herein
190 referred to as the Middle Permian blocky unit (Figs. 4, S2a,b). Limestone olistoliths range in size
191 from tens of meters to kilometers in diameter. Similar blocky units are known from the Upper
192 Karakaya Complex in the western part of the Sakarya Zone (Pickett and Robertson, 1996; Okay
193 and Göncüoğlu, 2004; Robertson and Ustaömer, 2012). The matrix in all these blocky units of the
194 Upper Karakaya Complex in the western part of the Sakarya Zone is Late Triassic in age, as can
195 be inferred from the ages of the youngest detrital zircons (Ustaömer et al., 2016). However, all
196 available detrital zircon ages from the matrix of the blocky unit are ≥ 294 Ma (earliest Permian,
197 $n=360$, this study). Hence, we have named this unit the Middle Permian blocky unit. This blocky
198 unit may be a discrete older part of the Upper Karakaya Complex. The largest exposure of this
199 unit, approximately 30 km long and up to 5 km wide, is found ca. 20 km to the north of Amasya.
200 Another exposure, ca. 10 km long and ca. 3 km wide, occurs around the town of Ladik. To the
201 north of the North Anatolian right-lateral strike-slip fault, there are also two discrete outcrops of
202 this blocky unit. Our descriptions here relate to two outcrops south of the North Anatolian Fault.
203 The base of the unit is not exposed. The internal stratigraphy of the blocky unit is obscure (Fig.
204 S2a). Layering is locally recognizable only in limestone. In the limestones there are clastic
205 interlayers up to 20 cm thick. The Middle Permian blocky unit is unconformably overlain by
206 either Lower Jurassic clastic rocks or Ammonitico-Rosso facies limestones (Fig. 3).

207 The Jurassic clastic rocks unconformably overlie the low-grade Permo-Triassic
208 metamorphic rocks of the Tokat Massif, and grade upward into Upper Jurassic and Lower

209 Cretaceous limestones (Figs. 3 and 4). The Early to Late Jurassic volcanic and volcanoclastic
210 rocks are confined to the Jurassic clastic successions located north of the Jurassic magmatic front
211 (Fig. 4). The total thickness of the clastic series south of Amasya is over 100 m. The lowermost
212 horizons (up to 15 m thick) consist of conglomerate grading upwards to sandstone and minor
213 siltstone. Individual layers are 20 to 80 cm thick. The clasts in the conglomerates range in
214 diameter from 2 to 20 cm and are composed mainly of chert, phyllite and metabasite. To the
215 northwest of Göynücek, the Lower Jurassic sandstones (ca. 60 m. thick) unconformably overlie
216 the retrogressed blueschist-facies rocks, and grade conformably upward to Upper Jurassic-Lower
217 Cretaceous chert-bearing, thin-bedded limestone.

218

219 **PETROGRAPHY**

220 In this study, we have studied detrital zircons from six sandstone samples collected over an area
221 of about 1100 km². Three of them come from the Middle Permian sandstones (T290A, T320 and
222 T356B), and three from the Lower Jurassic sandstones (samples T239, T267 and T295) (Figs. 3
223 and 4; Table S1). The Lower Jurassic sandstone samples were taken from the lowermost horizons
224 of the Lower Jurassic clastic sequence. The stratigraphic position of the Middle Permian
225 sandstones is difficult to deduce because the internal structure is unclear, and the base of the
226 Middle Permian blocky sequence cannot be observed.

227

228 **The Middle Permian Sandstones**

229 *Sample T290A* is a poorly sorted lithic arenite (matrix < 10 vol.%), comprising quartz (50-
230 60 vol.%) and minor K-feldspar (5 vol.%) and plagioclase (5 vol.%), and lithic fragments (ca. 30

231 vol.%; Fig. S3a). Lithic fragments consist mainly of fossiliferous limestone and minor amounts
232 of andesite and granite. Metamorphic rock fragments are rare. Myrmekitic and micrographic
233 microstructures are preserved in granite fragments. Quartz grains are predominantly
234 polycrystalline. The grains have an angular to subangular shape, and the grain size ranges from
235 50 to 300 μm , which indicates the poorly sorted nature of sandstone. All these features suggest
236 poor textural and mineralogical maturity. *Sample T320* is a poorly sorted, matrix-supported (ca.
237 30 vol.% matrix) lithic greywacke, comprising quartz (ca. 30 vol.%) and minor biotite (partially
238 chloritized), muscovite, K-feldspar, plagioclase and lithic fragments (ca. 30 vol.%; Fig. S3b).
239 Lithic fragments are predominantly limestone and minor andesite and granite. Metamorphic rock
240 fragments are minor. The grains mostly have an angular to subangular shape. Therefore, the
241 textural and mineralogical maturity is poor. *Sample T356B* is from an about 10 cm thick loose
242 sand interlayer within a Middle Permian limestone block. Thus, the sandy interlayer is interpreted
243 as contemporaneous with the limestone, in marked difference to samples T290A and T320, which
244 represent the surrounding matrix of limestone olistoliths.

245

246 **The Lower Jurassic Sandstones**

247 *Sample T239* is a poorly sorted Jurassic lithic arenite (matrix < 15 vol%), comprising
248 quartz (15-20 vol%), calcite (15-20 vol.%), and rock fragments (50-60 vol.%; Fig. S3c). Lithic
249 fragments were derived predominantly from limestone and subordinately phyllite, mica-schist,
250 andesite, granophyre and granite. Lithic fragments tend to be more rounded than quartz grains.
251 *Sample T267* is a poorly sorted lithic arenite similar to sample T239 (Fig. S3d). The grains are
252 dominated by lithic fragments (ca. 60 vol%), which are represented by limestone, greenschist,
253 phyllite/mica schist, calc phyllite, serpentinite, andesite, granite and polycrystalline quartz.

254 Metamorphic rock fragments are more common than igneous ones. Quartz (15-20 vol.%),
255 epidote, calcite, biotite and muscovite occur as discrete minerals. *Sample T295* is a poorly sorted
256 lithic greywacke (matrix ca. 20 vol%), comprising lithic fragments (ca. 35 vol.%), quartz (ca. 20
257 vol.%), biotite, muscovite, K-feldspar and plagioclase in a calcite cement/matrix (ca. 30 vol.%;
258 Figs. S3e-f). Lithic fragments are from phyllite/mica schist, andesite, granophyre, granite and
259 serpentinite. Overall, the grains have an angular to subangular shape.

260 In summary, both the Middle Permian and Lower Jurassic sandstones are poorly sorted
261 and lack textural and mineralogical maturity. The lithic fragments ranging from granitic to
262 granophyric rocks, and the abundance of biotite flakes particularly in the Lower Jurassic
263 sandstones suggest that a major part of the grains came from a continental area, as granitic to
264 granophyric rocks are missing in the Tokat Massif. Metamorphic rock fragments are more
265 common in the Lower Jurassic sandstones.

266

267 ANALYTICAL TECHNIQUES

268 Detrital zircons were extracted from sandstone samples weighing approximately 3 to 5 kg
269 using standard mineral separation techniques such as cracking, sieving, washing, drying,
270 magnetic and heavy mineral separation at the Eurasian Institute of Earth Sciences (Istanbul
271 Technical University). Handpicked zircons under a binocular microscope were mounted in epoxy
272 resin and polished down to roughly half thickness. Polished mounts were then photographed
273 using a scanning electron microscope equipped with a cathode luminescence (CL) detector at the
274 Geological Engineering Department of Hacettepe University in Ankara. Cathode luminescence

275 (CL) and backscattered electron images helped visualize the internal structures of the zircon
276 grains and the presence of inclusions prior to isotopic analysis.

277 U–Pb analyses and trace element compositions of zircon were determined simultaneously
278 by laser ablation-inductively coupled plasma-mass spectrometry (LA-ICP-MS). The analyses
279 were performed at the Institute of Geochemistry and Petrology, ETH Zurich (Eidgenössische
280 Technische Hochschule Zürich, ETHZ), Switzerland, using a RESolution (ASI/Applied Spectra)
281 excimer (ArF) 193 nm laser ablation system attached to an Element XR (Thermo) sector-field
282 ICP-MS. Lu-Hf analyses were obtained by laser ablation-multi-collection-inductively coupled
283 plasma-mass spectrometry (LA-MC-ICP-MS) at ETHZ, using a RESolution (ASI/Applied
284 Spectra) excimer (ArF) 193 nm laser ablation system attached to a Nu Plasma II (Nu Instruments)
285 multi-collector ICP-MS. Details about the instrumentation and analytical conditions can be found
286 in the Appendix and in Tables S2 and S3. Data from unknowns and reference materials are
287 presented in Tables S4 and S5. Concordia and frequency probability plots were produced using
288 ISOPLOT v.4.15 (Ludwig, 2003). The concordance of the ages was calculated using the ratio of
289 $^{206}\text{Pb}/^{238}\text{U}$ and $^{207}\text{Pb}/^{235}\text{U}$ ages. In this study, only the analyses with concordance between 90–
290 110% are considered. In the histograms, $^{206}\text{Pb}/^{238}\text{U}$ ages are used for zircons with ages <1 Ga,
291 while $^{207}\text{Pb}/^{206}\text{Pb}$ ages are used for zircons with ages >1 Ga. The probability curve shows the
292 mean peak age of the age group in a sample.

293

294 **RESULTS**

295 **Morphology and Internal Structure**

296 The zircons in the studied samples are characterized by (i) grain sizes ranging from 50 to
297 200 μm in the longitudinal direction, (ii) colors ranging from clear colorless, yellowish to violet,
298 and (iii) external shapes ranging from euhedral prismatic to wholly rounded (Fig. S4). Euhedral
299 prismatic zircon grains account for less than 15 % of the dated detrital zircon grains. The vast
300 majority of zircon grains (ca. 90 %) show well-developed oscillatory zoning along with sector
301 zoning. Metamict zircons are not recognized. Some grains appear to have inherited core-like
302 domains. Feldspar and apatite inclusions are common in zircon grains. The marginal domains of
303 the zircon grains were preferred for the measurements.

304 **Trace Element Compositions**

305 A total of 720 spot analyses have been performed on the detrital zircons from six
306 sandstone samples. In each sample, 120 spots were analysed (Table S4) to maximize
307 representativeness of the sample population (Vermeesch, 2004). A total of 616 spot analyses
308 yielded concordant U-Pb ages at 90–110 % [$(^{207}\text{Pb}/^{235}\text{U} \text{ age}) / (^{206}\text{Pb}/^{238}\text{U} \text{ age}) * 100$]. We only
309 consider the age values and trace element compositions of concordant spot analyses.

310 The zircon grains are mainly characterized by a steep heavy rare earth element-enriched
311 (REE) pattern, a positive Ce anomaly, and a negative Eu anomaly (Figs. S5a-f). There is no
312 apparent relationship between the age of the detrital zircons and REE characteristics, such as the
313 magnitude of the negative Eu anomaly (not shown). Out of 616 concordant analyses, only twelve
314 zircon grains show REE patterns with heavy REE depletion and varying degrees of negative Eu
315 anomaly, a feature of zircons equilibrated with garnet (Fig. S5g) (e.g., Rubatto, 2002). Some
316 zircon grains (16 grains) exhibit a steep REE pattern with minor Eu anomaly, suggesting growth
317 from magmas that did not experience significant plagioclase fractionation (Fig. S5h).

318 U-Pb Zircon Ages

319 In the Middle Permian sandstone samples, the $^{206}\text{Pb}/^{238}\text{U}$ ages of the detrital zircon grains
320 range from 294 to 2913 Ma (earliest Permian to Mesoarchean after Cohen et al., 2013 updated)
321 (Figs. 5a-c; Table S4). The youngest detrital zircon population in all three samples is earliest
322 Permian in age (299–294 Ma) consistent with the paleontological dates of the limestone
323 olistoliths. In all Middle Permian sandstone samples, the $^{206}\text{Pb}/^{238}\text{U}$ ages of the detrital zircon
324 grains define marked age clusters peaking at 318, 324 and 325 Ma (Late Carboniferous). The
325 main age population in samples T290A and T320A (53 and 57% of all concordant zircons) is
326 Neoproterozoic to latest Mesoproterozoic with noticeable clusters at 562–555, 634–629 and ca.
327 1025 Ma (Figs. 5a-b). In contrast, zircons older than Paleozoic are subordinate (ca. 25%) in
328 sample T356B, where the dominant age peak is at 392 Ma (Middle Devonian) (Fig. 5c).

329 In the Lower Jurassic sandstone samples, the age of the detrital zircons ranges from 195
330 to 2698 Ma (Early Jurassic to Neoarchean) (Figs. 5d-f; Table S4). All samples consistently
331 display noticeable age clusters at 250–233 and 318–316 Ma. In addition, there are marked age
332 clusters peaking at 380 and 383 Ma in samples T239 and T267, respectively. Only sample T239
333 has an additional age peak located at 441 Ma. The Paleozoic to early Mesozoic zircons make up
334 66% of all the concordant zircon grains in sample T295, and 37 and 44% in samples T239 and
335 T267, respectively. Similar to the Middle Permian sandstones, the Lower Jurassic sandstones
336 have age clusters at 581, 650–604 and 969–1027 Ma (late Neoproterozoic to latest
337 Mesoproterozoic). Samples T239 and T267 are further characterized by non-negligible mid-
338 Paleoproterozoic to Neoarchean populations (ca. 15-29% of all concordant zircons; Figs. 5d-e).
339 In sample T295, only 6 out of 105 grains have $^{207}\text{Pb}/^{206}\text{Pb}$ ages >1500 Ma (Fig. 5f).

340 In summary, the detrital zircon age spectra from both the Lower Jurassic and Middle
341 Permian sandstones contain variable amounts of Phanerozoic zircons that define distinct age
342 clusters in the range of 250–233, 325–316 and 392–380 Ma. The combination of all detrital
343 zircon age data suggests that the most pronounced clusters are at 325–316 Ma (mainly Late
344 Carboniferous), followed by 250–230 Ma (mainly Early to Middle Triassic). The age cluster at
345 393–380 Ma (mainly Middle Devonian) is the least pronounced one, and a subdued age peak at
346 ca. 441 Ma (Early Silurian) is present only in one sample.

347 **Lu-Hf Isotopic Compositions**

348 Lu-Hf isotopic compositions of the 478 detrital zircon grains from six samples were
349 measured (Table S5). In each sample, at least 70 spots on the zircon grains with concordant U-Pb
350 ages were analyzed. The results are shown on $^{206}\text{Pb}/^{238}\text{U}$ zircon ages (Ma) versus time-corrected
351 ϵHf values in Figures 6a-b.

352 The initial ϵHf values of the dated zircon grains show a large variation from -26 to +14.
353 Although detrital zircons with Triassic ages exhibit initial ϵHf values from -3 to +10, the negative
354 values make up only 12.5% of this age population. On the other hand, Carboniferous zircons
355 have initial ϵHf values in the range of -12 to +13, where negative initial ϵHf values make up ca.
356 94 % and positive values are only shown by the zircons with ages ≤ 314 Ma. Middle Devonian
357 zircons display initial ϵHf values ranging from -9 to +7 with negative initial ϵHf values
358 accounting for 76 %. Silurian zircons are characterized by initial ϵHf values of -5 to +8 with
359 positive initial ϵHf values making up ca. 60%. It is noteworthy that the detrital zircons from the
360 Middle Permian and Lower Jurassic sandstones show different ranges of ϵHf values for a given
361 age for the Paleozoic era. For example, Devonian zircons from the Middle Permian sandstones
362 are characterized mainly by negative initial ϵHf values, and those from Lower Jurassic

363 sandstones mainly by positive ϵ_{Hf} values. The same trend is also observed in the latest
364 Carboniferous zircons. In addition, one Permian sample shows a very clear population at ca. 550
365 Ma with positive ϵ_{Hf} (around +10), which is lacking in the Lower Jurassic samples. Archean and
366 Proterozoic zircons from both Middle Permian and Lower Jurassic sandstones, on the other hand,
367 show the same range of initial ϵ_{Hf} .

368 To sum up, initial ϵ_{Hf} values of the detrital zircons vary widely from positive to negative
369 in both the Middle Permian and Lower Jurassic sandstones. The Triassic and Silurian zircons are
370 characterized primarily by positive initial ϵ_{Hf} values, while the Late Carboniferous and Middle
371 Devonian zircons are characterized primarily by negative initial ϵ_{Hf} values. The detrital zircons
372 from the Middle Permian and Lower Jurassic sandstones show different ranges of initial ϵ_{Hf}
373 values for the same age range during the Paleozoic era.

374

375 **DISCUSSION**

376 **Geochemical Constraints on Possible Sources of Detrital Zircons**

377 Th/U ratios of the dated zircon grains range from 0.01 to 1.54 (Figs. S6a-b; Table S4).
378 Only 16 zircon grains among 616 concordant analyses (ca. 2.6 %) have Th/U ratios less than
379 0.10. Zircons with Th/U ratios <0.10 are concentrated at 495–467 (late Cambrian-Ordovician)
380 and 573–745 Ma (middle to late Neoproterozoic). Commonly, zircons with a Th/U ratio <0.10
381 are considered to be metamorphic in origin, and zircons with a Th/U ratio >0.10 are igneous in
382 origin (e.g., Rubatto, 2002; Hoskin and Schaltegger, 2003). Based on the compilation of the
383 metamorphic zircon compositions and phase equilibrium modeling in metapelitic systems,
384 Yakymchuk et al. (2018), however, showed that the Th/U ratio of suprasolidus metamorphic
385 zircon is controlled by (i) U and Th concentrations in the system, (ii) the amount of monazite, and

386 (iii) the timing of zircon crystallization. Metamorphic zircons that crystallized at or near wet
387 solidus in the presence of monazite are predicted to have Th/U ratios < 0.1 , while metamorphic
388 zircons that crystallized under open-system conditions at elevated temperatures in the absence of
389 monazite are predicted to have Th/U ratios > 0.1 . To summarize, all zircon grains with Th/U
390 ratios < 0.1 are probably of metamorphic origin grown in the presence of monazite, but not all
391 metamorphic zircons have Th/U ratios < 0.1 .

392 U/Yb ratios of the zircon grains range from 0.1 to 47.2, with average values between 0.8
393 and 1.3 in different samples (Figs. S6c-d). Overall, zircons grown in magmas from enriched
394 mantle and crustal sources mostly show elevated U/Yb ratios (ca. > 0.1) compared to those from
395 normal mid-ocean ridge magmas (Grimes et al., 2015). Nb/Yb ratios range from 0.001 to 0.483,
396 with average values between 0.008 and 0.013 (Figs S6e-f). Thus, the majority of the dated zircon
397 grains plot above the mantle array on the Nb/Yb versus U/Yb diagram after Grimes et al. (2015)
398 (Fig. 7a). Forty zircon grains out of 616 concordant grains (7%) fall within the field of mantle
399 zircon array which is defined by the zircons of mid-ocean ridges, ocean islands and plume-
400 influenced settings. Only eight zircon grains out of 40 yielded Phanerozoic ages of 225–211 and
401 433–428 Ma (Late Triassic and Silurian). Thus, the overwhelming majority of dated zircon
402 grains are compositionally similar to those from convergent margin granitoids. On the Hf versus
403 Ti diagram after Laurent et al. (2022) (Fig. 7b), the zircons fall within the fields defined by the
404 zircons from magmatic arc to post-orogenic I-type granites.

405 Based on the above considerations and the internal structures of dated zircon grains (Fig.
406 S4), we conclude that the dated zircon grains, regardless of their age, were predominantly derived
407 from convergent margin igneous rocks, and only a small fraction might be of metamorphic and
408 mid-ocean ridge and ocean island basaltic origin (ca. $< 10\%$).

409 **Paleozoic-Early Mesozoic Magmatic Flare-ups**

410 The combination of all detrital zircon ages from the Middle Permian and Lower Jurassic
411 sandstones defines three major age peaks at 240, 321 and 391 Ma, and smaller age peaks at 212,
412 430 and 475 Ma (Figs. 8a-b). Comparable age peaks (238, 312 and 393 Ma) are delineated by the
413 detrital zircons of (meta-)sandstones, collected over an area of 28 000 km², within the Late
414 Triassic accretionary complexes in the western part of the Sakarya Zone, ca. 600 km west of the
415 Tokat Massif (Figs. 7c-d; Ustaömer et al., 2016). A limited set of detrital zircon ages from Lower
416 to Upper Jurassic clastic rocks in the Gümüşhane area, ca. 300 km east of Tokat Massif,
417 uniformly define age clusters at 204–199 and 320–310 Ma (Figs. 2 and S7a-b) (Akdoğan et al.,
418 2018; Liu et al., 2022). Although the Carboniferous clusters entirely overlap with those in this
419 study and in Late Triassic accretionary complexes from the western part of the Sakarya Zone
420 (Ustaömer et al., 2016), the Triassic zircon age peak occurs at 204–199 Ma (latest Triassic-
421 earliest Jurassic) rather than at 250–230 Ma (Early to Late Triassic), which is comparable to the
422 minor peak in sample T239 (Fig. 5d). Furthermore, there is no Middle Devonian age peak.
423 However, detrital zircons from an Early Carboniferous low-grade metapsammite from the
424 Demirözü area, ca. 40 km to the southeast of Gümüşhane, displays a pronounced Middle
425 Devonian age cluster peaking at 393 Ma (sample BP36 in Dokuz et al., 2022) (Fig. S7c). Detrital
426 zircon U-Pb zircon ages from the central part of the Sakarya Zone and Crimea show some
427 marked differences from the eastern and western parts of the Sakarya Zone such as (i) the
428 presence of a pronounced Early Permian age peak (291–289 Ma) (Figs. S7d-e), (ii) a significant
429 abundance of Paleoproterozoic and Meso- to Neoproterozoic zircons, and (iii) the sporadic
430 occurrence of the zircons in the age range 1100 and 1700 Ma (Okay et al., 2013; Akdoğan et
431 al., 2017; Kuznetsov et al., 2019; Nikishin et al., 2020). These differences are also reflected in the

432 age data of the detrital zircons from Lower Cretaceous turbidites in the region which have been
433 attributed to a source in the East European Craton before the opening of the Black Sea during the
434 Late Cretaceous (Okay et al., 2013; Akdoğan et al. 2017, 2019). Liu et al. (2022), on the other
435 hand, suggest that there was no exchange of detritus across the Eastern Black Sea basin during
436 the Middle Jurassic–early Eocene, and the Eastern Black Sea basin was probably rifted by the
437 Middle Jurassic as a back-arc basin. The source of Early Permian zircons can be ascribed to the
438 local granites of Early Permian age in the Central Pontides (e.g. Nzegge et al., 2006). The other
439 age clusters are comparable to those defined by the detrital zircons from the Middle Permian and
440 Lower Jurassic clastic rocks of the Tokat Massif.

441 To sum up, available detrital zircon U-Pb age data from the Permian, Late Triassic and
442 Jurassic clastic rocks from the Sakarya Zone consistently define major age clusters at 250–230,
443 326–310 and 400–380 Ma, as well as less pronounced clusters at 215–195, 455–430 and
444 480–470 Ma. The presence of these major age clusters is also supported by the detrital zircon
445 ages from Upper Cretaceous and Middle Eocene clastic rocks throughout the Sakarya Zone (Figs.
446 8e-f, S7) (e.g. Okay et al., 2013; Akdoğan et al., 2017, 2019; Mueller et al., 2019, 2022; Liu et
447 al., 2022). These age clusters correspond to the magmatic flare-ups in the Sakarya Zone. Given
448 the uncertainties in the age data, these major magmatic flare-ups lasted ca. 15 to 20 Ma and were
449 separated by magmatic lulls lasting ca. 15 to 60 Ma.

450 **Possible Provenance of Early Mesozoic-Paleozoic Zircons**

451 There are no well-documented and confirmed Triassic magmatic arc rocks in the pre-
452 Jurassic basement outcrops in the Sakarya Zone, despite the common presence of Triassic detrital
453 zircons in the Late Triassic accretionary complexes and in the Lower Jurassic sandstones (Okay
454 and Nikishin, 2015, Ustaömer et al., 2016, this study). The only reported Triassic igneous rocks

455 are anorogenic alkaline to tholeiitic (meta-)gabbros in the Late Triassic accretionary complexes
456 and Late Cretaceous ophiolitic mélanges (e.g. Eyüboğlu et al., 2011, 2018; Çelik et al., 2019b).
457 We, however, consider it unlikely that the Triassic zircons in our data set were derived from
458 Triassic gabbroic rocks within the Permo-Triassic accretionary complexes, on the basis of zircon-
459 poor nature of the gabbroic rocks and trace element compositional features of the dated zircons
460 (Fig. 7). Based on the presence of Triassic igneous rocks from the bore-hole data from the
461 Scythian platform, Okay and Nikishin (2015) proposed that the Triassic magmatic arc lies buried
462 under the Cenozoic cover of the Scythian platform (Fig. 2), which was adjacent to the Pontides
463 before the Late Cretaceous opening of the Black Sea. The Middle to Late Permian time (264–252
464 Ma) represents a short phase of magmatism in the Istanbul Zone (Bozkurt et al., 2013; Aysal et
465 al., 2018; Babaoğlu et al., 2023) (Fig. 2). This magmatism is somewhat older than the postulated
466 Triassic magmatic flare-up (250–230 Ma). Hence, we regard it improbable that the Triassic
467 zircons in the Latest Triassic accretionary complexes and Lower Jurassic sandstones originated
468 from the Istanbul Zone during Early Jurassic time. In conclusion, the derivation of the Early to
469 Middle Triassic zircons from the northern range prior to the opening of the Black Sea Basin
470 seems to be a conceivable possibility, as suggested by Okay and Nikishin (2015).

471 The Late Carboniferous magmatic flare-up (326–310 Ma) represents the most voluminous
472 and relatively well-documented one. Magmatic rocks showing similar ages as this flare-up are
473 batholiths and stocks throughout the Sakarya Zone and Caucasus, comprising mainly middle- to
474 high-K calc-alkaline I-type granites (Fig. 2; e.g., Topuz et al., 2010; Ustaömer T. et al., 2013;
475 Dokuz, 2011; Ustaömer P.A. et al., 2012; Kaygusuz et al., 2012, 2016; Rolland, 2017). Late
476 Carboniferous gabbroic rocks (326–322 Ma) are minor, and represented by relatively small mafic
477 to ultramafic intrusions, and were derived from middle to high-K calc-alkaline basic magmas

478 (Topuz et al., 2023). The magmatic flare-up event started ca. 5–8 Ma after the peak of the
479 regional HT-M to LP metamorphism. In some provenance studies, the Carboniferous age cluster
480 is located at 334–330 Ma (e.g., Mueller et al., 2019; Kuznetsov et al., 2019), which corresponds
481 to the peak of the HT-M to LP metamorphism throughout the Sakarya Zone and Caucasus and
482 NW Iran (Figs. 2 and 3) (Topuz et al., 2004b; Mayringer et al., 2011; Ustaömer T. et al., 2013;
483 Rolland et al., 2016; Roland, 2017; Moazzen et al., 2020). The initial ϵ_{Hf} values of both the Late
484 Carboniferous detrital zircons and the Late Carboniferous granites entirely overlap (Fig. 6b). This
485 similarity is also reinforced by fully negative values of the initial ϵ_{Nd} values of the Late
486 Carboniferous granites.

487 In contrast to the Late Carboniferous igneous rocks, the Middle Devonian igneous rocks
488 are documented locally from the Sakarya Zone (Okay et al., 2006; Aysal et al., 2011; Sunal,
489 2011; Topuz et al., 2020; Karlı et al., 2020; Dokuz et al., 2022). In recent years their number has
490 steadily increased with the dating of metaigneous rocks within the Early Carboniferous HT-M to
491 LP metamorphic units. The Middle Devonian rocks are represented by biotite \pm hornblende-
492 bearing and muscovite \pm biotite granites with U-Pb zircon igneous crystallization ages of
493 404–380 Ma. The relatively pronounced age clusters at 400–380 Ma in the detrital zircon age
494 histograms (Figs. 8a-d) suggest that the Early to earliest Late Devonian igneous rocks must be
495 more common than documented. The predominantly negative values of the initial ϵ_{Hf} values of
496 the Middle Devonian detrital zircons (ca. 76%) are consistent with the widespread occurrence of
497 the Middle Devonian muscovite \pm biotite granites. The Devonian zircons in the Middle Permian
498 sandstones have predominantly negative initial ϵ_{Hf} values, while those in the Lower Jurassic
499 sandstones have predominantly positive initial ϵ_{Hf} values (Fig. 6b). This quite contrasted isotopic
500 signature suggests that the Middle Permian and Lower Jurassic sandstones do not have the same

501 provenance and/or that the Middle Devonian magmatism was characterized by bimodal processes
502 involving either reworking of older crust or new growth from depleted mantle-like sources. In
503 any case, there were predominantly juvenile magmatic rocks in the catchment area when the
504 Lower Jurassic sandstone was formed.

505 The Late Ordovician-Silurian detrital zircon age peak is apparent only in some
506 provenance studies (Figs. 8b and 8f and S7d-f) (Okay et al., 2013; Akdoğan et al., 2017;
507 Kuznetsov et al., 2019; Mueller et al., 2022, this study). So far, Silurian igneous rocks are known
508 from the western part of the Sakarya Zone, where they are represented mainly by anorogenic
509 alkaline and tholeiitic amphibolite and subordinately metagranite with igneous crystallization
510 ages of 440–420 Ma (Topuz et al., 2020; Karşlı et al., 2020). The basic rocks were derived
511 mainly from juvenile material, while acidic rocks were derived from magmas which involved
512 substantial reworked material (Fig. 6b). Local appearance of the Silurian age peak can be a bias
513 mainly due to the basic nature of the Late Ordovician-Silurian igneous rocks.

514 Detrital zircon ages from the Middle Permian and Lower Jurassic sandstones define a
515 minor subdued peak at 475 Ma (Early Ordovician). Similar age clusters are also found in the
516 detrital zircon age data of Akdoğan et al. (2017) and Mueller et al. (2022). To date, Ordovician
517 igneous rocks have been reported only from the Armutlu Peninsula in the western Sakarya Zone
518 (Okay et al., 2008) and from the Kurtoğlu metamorphic area in the eastern Sakarya Zone (Dokuz
519 et al., 2022). Based on Th/U ratio ≤ 0.1 , some detrital zircon grains with Early Ordovician ages
520 are thought to have a possible metamorphic origin, which is consistent with the data presented in
521 Ustaömer et al. (2013). However, Early Ordovician metamorphism in the Sakarya Zone is still
522 unknown.

523 **Possible Causes of the Paleozoic-Early Mesozoic Flare-ups**

524 There are only a few studies dealing with the Paleozoic to Early Mesozoic evolution of
525 the Sakarya Zone (e.g. Okay et al., 2006; Okay and Topuz 2017; Topuz et al., 2020; Ustaömer et
526 al. 2012, 2013; Dokuz et al., 2017, 2022; Eyüboğlu et al., 2010, 2018; Karslı et al., 2020). There
527 is a general consensus that the Sakarya region is a block of Gondwana origin, based on the
528 widespread presence of Neoproterozoic zircons in pre-Jurassic metaclastic rocks (Ustaömer et al.,
529 2012, 2013). However, the timing of rifting from Gondwana in the south, and accretion to
530 Laurussia in the north are highly debated. Several studies (e.g., Şengör and Yılmaz, 1981; Şengör
531 et al., 2019; van Hinsbergen et al., 2020) suggest that the Sakarya Zone first separated from the
532 northern margin of Gondwana during Permo-Triassic time. On the other hand, Karslı et al. (2020)
533 and Dokuz et al. (2022) argue that the pre-Jurassic basement of the Sakarya Zone contains
534 domains that detached from the northern margin of Gondwana at different times such as the
535 Ordovician and the Late Devonian, and the pre-Jurassic basement of the Sakarya Zone contains
536 domains derived both Avalonia and Armorican Terrane Assemblage. Both proposals are
537 considered unlikely based on the following arguments. As mentioned above, the Izmir-Ankara-
538 Erzincan suture represents the trace of a long-lived oceanic domain at least from the Silurian to
539 Late Cretaceous on the basis of the age of the accretionary complexes and deep-marine
540 sedimentary blocks therein (e.g. Okay et al., 2013, 2020; Topuz et al., 2013). Moreover, the
541 Middle Paleozoic-Early Mesozoic stratigraphy of the Sakarya Zone and the Anatolide-Tauride
542 Block, the Arabian Platform, differ significantly (Fig. S1). The latter proposal suggests an
543 opening of Paleo-Tethys to the north of the Rheic Ocean, which contradicts the areal distribution
544 of the Paleo-Tethyan accretionary complexes in the Sakarya Zone and with configurations of the
545 oceanic domains in the commonly accepted paleogeographic reconstructions (e.g. Stampfli and
546 Borell, 2002). So far, no area has been identified that has a large number of detrital zircons with

547 ages ranging from 1100 to 1750 Ma inside the basement units of the Sakarya Zone, that could
548 represent part of Avalonia (Figs. 8 and S7).

549 Below we discuss the possible drivers of Paleozoic to early Mesozoic magmatic flare-ups
550 in the Sakarya Zone in the context of the following constraints: (i) The Sakarya Zone is a
551 Gondwanian continental fragment, and forms the eastern extension of the Armorican Terrane
552 Assemblage (Winchester and the Pace TMR Network Team, 2002; Okay et al., 2006; Ustaömer
553 et al., 2012; Okay and Topuz, 2017), (ii) the Sakarya Zone rifted from the northern margin of
554 Gondwana probably during the Late Ordovician-Silurian, and accreted to Laurussia during the
555 Carboniferous (e.g., Ustaömer et al., 2013; Okay and Topuz, 2017; Topuz et al., 2020), and (iii)
556 the limited Paleozoic and early Mesozoic igneous rocks in the Anatolide-Tauride Block are ruled
557 out as potential source since the Izmir-Ankara-Erzincan suture represents the trace of an oceanic
558 domain which existed from the middle Paleozoic to the end-Mesozoic (e.g., Topuz et al., 2013;
559 Okay et al., 2020). Therefore, the Paleozoic to early Mesozoic magmatic flare-ups cannot be
560 explained by processes along a single subduction zone. The processes leading to detachment
561 from the northern margin of Gondwana, northward drift, and accretion to the southern margin of
562 Laurussia should be considered. As a reference point, we use the Late Carboniferous-Permian
563 paleogeographic reconstruction at the end of the Variscan Orogeny, which consistently shows an
564 easterly widening oceanic embayment (Fig. 9a) (e.g. Stampfli and Borell, 2002; von Raumer et
565 al. 2013). As the continental collision is succeeded by large-scale strike-slip faulting and the
566 formation of intracontinental basins in Central Europe (e.g. Corsini and Rolland, 2009), the
567 Sakarya and Istanbul zones were located at the southern margin of Laurasia. Below, we discuss
568 the possible causes of the magmatic flare-ups from the youngest one to the oldest one (Figs. 9b-
569 g).

570 Compelling evidence for the existence of subduction during Permo-Triassic times comes
571 from the widespread Permo-Triassic accretionary complexes including Triassic eclogites,
572 blueschists and Permian ophiolites (e.g. Pickett and Robertson, 1996; Okay and Monie, 1997;
573 Okay et al., 2002, 2020; Okay and Göncüoğlu, 2004; Topuz et al., 2004b, 2014, 2018; Robertson
574 and Ustaömer, 2011). Thus, the Triassic magmatic flare-ups at 250–230 and 215–198 Ma are
575 related to the northward subduction of Paleo-Tethys beneath the Sakarya Zone (Figs. 9b-c). The
576 widespread presence of anorogenic alkaline to tholeiitic metagabbroic rocks in the Late Triassic
577 accretionary complexes point to the accretion of a seamount chain or an oceanic plateau (Pickett
578 and Robertson, 1996; Sayit and Göncüoğlu, 2009). Consequently, the latest Triassic-earliest
579 Jurassic minor flare-up might be related to slab steepening following the accretion of a seamount
580 chain or an oceanic plateau. This situation would lead to the migration of a magmatic front from
581 the north to the south.

582 Late Carboniferous magmatic flare-up occurred 5-8 Ma after the peak of HT-M to LP
583 metamorphism in the Sakarya Zone, and took place during the exhumation of HT-M to LP
584 metamorphic rocks in an extensional setting (Topuz et al., 2023). The drastic change in U-Pb
585 zircon age spectra of the Istanbul Zone (Avalonia) as of Carboniferous time provides conclusive
586 evidence that the accretion of the Sakarya Zone to Laurussia during Early Carboniferous by the
587 consumption of the Rheic ocean (Okay and Topuz, 2017; Akdoğan et al., 2022). The Late
588 Carboniferous magmatic flare-up is tentatively ascribed to the removal of the lowermost part of
589 the lithosphere by convective thinning (Topuz et al., 2022) (Figs. 9d-e). Recent discoveries of
590 Early Carboniferous high-pressure metamorphic rocks in northwestern Iran indicate that the
591 southern margin of the Sakarya Zone and the Caucasus was active during Early Carboniferous
592 (e.g. Rosetti et al., 2017; Wan et al., 2021) (Fig. 2). However, it is unclear whether this

593 subduction was short-lived or continuous from the Early Carboniferous to the Middle Permian. It
594 is difficult to assess the relative contributions of active subduction and accretion to Late
595 Carboniferous magmatic flare-up. Seeing that the *HT-M* to *LP* metamorphism throughout the
596 Sakarya Zone, the Caucasus and NW Iran occurred at 335–330 Ma (e.g. Topuz et al., 2004a;
597 Mayringer et al., 2011; Ustaömer et al., 2013; Rolland et al., 2016; Roland, 2017; Moazzen et al.,
598 2020), and the high-volume magmatism occurred during the exhumation of the *HT-M* to *LP*
599 metamorphic rocks (Topuz et al., 2010, 2023), we argue that the removal of the lowermost parts
600 of the thickened lithosphere after the accretion to Laurussia seems a more conceivable trigger for
601 the Late Carboniferous flare-up (Figs. 9d-e). A similar scenario has been proposed for the Late
602 Carboniferous magmatism in the French Massif Central, part of the Armorican Terrane
603 Assemblage in Central Europe (Fig. 1; Laurent et al. 2017; Vanderhaeghe et al. 2020).

604 To date, no Devonian accretionary complexes in the form of high-pressure rocks and
605 ophiolites have been reported. Middle Devonian igneous biotite ± hornblende granites display
606 subduction-related geochemical affinity (Aysal et al., 2012). Paleogeographic reconstructions
607 consistently show that the northern margin of the Armorican Terrane Assemblage was bound by
608 a south-vergent subduction zone (Stampfli and Borell, 2002; von Raumer et al., 2013). Hence, we
609 cautiously ascribe the Middle Devonian flare-up to the southward subduction of the Rheic ocean
610 beneath the Sakarya Zone during the northward drift (Fig. 9f).

611 Middle Ordovician-Silurian (460-430 Ma) probably represents the time of the rifting of
612 the Sakarya Zone from the northern margin of Gondwana (Fig. 9g), which is inferred from (i) the
613 within-plate geochemical features of amphibolite with Silurian protolith ages in the Sarıcakaya
614 Massif (Fig. 2), and (ii) the presence of Late Silurian to Devonian deep-sea sedimentary blocks in

615 the Paleo-Tethyan accretionary complexes in the western part of the Sakarya Zone (Topuz et al.,
616 2020, and the references therein).

617 In conclusion, the locally recorded Late Ordovician-Silurian magmatic flare-up was likely
618 caused by the rifting of the Sakarya Zone from the northern margin of Gondwana. The Middle
619 Devonian magmatic flare-up and subsequent accretion to Laurussia during the Early
620 Carboniferous were caused by the northward drift associated with the southward subduction of
621 the Rheic ocean beneath the northern margin of Sakarya Zone. The most voluminous magmatic
622 flare-up occurred during the Late Carboniferous and was most likely related to the loss of the
623 lowermost sections of the thickened lithosphere. The southern margin of the Sakarya Zone
624 became active following the accretion to Laurussia to the north. The Triassic magmatic flare-up,
625 the most juvenile one among the documented ones in this study, were connected to the Paleo-
626 Tethys' northward subduction beneath the Sakarya Zone.

627

628 **Comparison with the Armorican Terranes**

629 Below, we make a preliminary comparison of the Paleozoic-Early Mesozoic detrital
630 zircon age clusters of the Sakarya Zone with those of the Greater Caucasus in the east, the
631 Balkans in the west and southern France in Europe (Fig. 1). All of these areas are part of the
632 Armorican Terrane Assemblage. Similar to the Sakarya zone, the Greater Caucasus and the
633 Balkans were also involved in Alpine orogeny, although southern France was outside the Alpine
634 orogenic belt. The main difficulty in making the comparisons is that provenance studies based on
635 U-Pb-zircon dating have mainly been performed on young sedimentary rocks such as the
636 Oligocene to Miocene and recent clastic rocks (Allen et al., 2006; Vincent et al., 2013; Abbo et

637 al., 2020), rather than basement rocks or older clastic rocks unconformably overlying basement
638 rocks.

639 A Middle to Upper(?) Jurassic sandstone sample from the Greater Caucasus shows U-Pb
640 zircon age clusters peaking at 164, 242, 319 and 444 Ma (Allen et al., 2006) (Fig. 10a). Abbo et
641 al. (2020) dated the detrital zircons from beach placer samples taken from the estuaries of three
642 major rivers such as Strymon, Nestos and Evros that drain Serbo-Macedonian and Rhodope
643 massifs (Fig. 1). The detrital zircons yield zircon age clusters peaking at 245, 309 and 460 Ma
644 apart from the Mesozoic and Cenozoic ones (Fig. 10b). The Rhone River (southern France)
645 drains a significant part of the European Armorican terranes, only a small portion of which was
646 involved in Alpine orogeny (Fig. 1) (Avigad et al., 2022). The delta sands of the Rhone river
647 yield U-Pb zircon age clusters peaking at 309, 456 and 553 Ma (Fig. 10c).

648 The Late Carboniferous magmatic flare-up is the most characteristic feature of the entire
649 Armorican Terrane Assemblage. Likewise, Late Ordovician-Silurian magmatic flare-up which is
650 recorded in some provenance studies in the Sakarya Zone is widespread. The Triassic magmatic
651 flare-up seems to be restricted of the parts of the Armorican Terrane Assemblage that was later
652 involved in Alpine orogeny. The Middle Devonian flare-up is local, confined to the Sakarya
653 Zone.

654

655 **CONCLUSIONS**

656 U-Pb detrital zircon ages from Middle Permian and Lower Jurassic sandstones from the Tokat
657 Massif in conjunction with the literature data define the presence of three episodes of Paleozoic-
658 Early Mesozoic high-volume magmatism in the Sakarya Zone: Triassic (250–230 Ma), Late

659 Carboniferous (325–310 Ma) and Middle Devonian (400–380 Ma). Among the magmatic flare-
660 ups, the Late Carboniferous one is the most voluminous one, followed sequentially by the
661 Triassic, and the Middle Devonian ones. As the Sakarya Zone is a Gondwana-derived block that
662 was successively involved in Variscan and Alpine orogenies, these magmatic flare-ups cannot be
663 explained by processes along a single subduction zone. Detachment from the northern margin of
664 Gondwana and collage with the Laurussia should also be considered. The Late Carboniferous
665 flare-up event is well-documented in outcrop, and is marked by the formation of batholiths which
666 postdate the peak of HT-M to LP metamorphism by at least 5 to 8 Ma. It is ascribed to the
667 convective thinning of the lowermost part of the thickened lithosphere following the accretion of
668 the eastern Armorica with Laurussia. The Triassic magmatic flare-up event represents the most
669 juvenile crust formation. The widespread occurrence of Permo-Triassic accretionary complexes
670 suggests that the Triassic magmatic flare-up occurred in an active subduction setting, ascribed to
671 the northward subduction of the Tethys. On the other hand, related Triassic magmatic arc rocks in
672 the basement exposures of the Sakarya Zone have not been defined so far. The Middle Devonian
673 magmatic flare-up event is tentatively ascribed to the southward subduction of the Rheic oceanic
674 lithosphere beneath the Sakarya Zone. The Triassic and Late Carboniferous high-volume
675 magmatism is also a characteristic feature of the Balkans and the Caucasus. The Middle
676 Devonian one seems confined to the Sakarya Zone. Along with the Late Carboniferous flare-up,
677 the Late Ordovician-Silurian flare-up, which is locally recorded in the Sakarya Zone, is
678 representative of the Armorican Terrane Assemblage as a whole.

679 **ACKNOWLEDGMENTS**

680 We have benefited from the constructive reviews of Yann Rolland, Nurettin Kaymakçı and two
681 anonymous referees, and discussions with Aral I. Okay. We gratefully acknowledge the help of

682 Cemre Ay, İnal Demirkaya, Merve Dilbaz and Mutlu Özkan during mineral separation. This
683 study has been financially supported by a research grant from the scientific and technological
684 research council of Turkey (TÜBİTAK #116Y234) and the research foundation of the Istanbul
685 Technical University (İTÜ BAP #39758).

686 REFERENCES CITED

687 Abbo, A., Avigad, D., Gerdes, A., 2020, Crustal evolution of peri-Gondwana crust into present
688 day Europe: The Serbo-Macedonian and Rhodope massifs as a case study: *Lithos*, v. 356,
689 105295, <https://doi.org/10.1016/j.lithos.2019.105295>.

690 Akdoğan, R., Okay, A.I., and Dunkl, I., 2018, Triassic-Jurassic arc magmatism in the Pontides as
691 revealed by the U-Pb detrital zircon ages in the Jurassic sandstones of northeastern Turkey:
692 *Turkish Journal of Earth Sciences*, v. 27, p. 89–109, <https://doi.org/10.3906/yer-1706-19>.

693 Akdoğan, R., Okay, A.I., and Dunkl, I., 2019, Striking variation in the provenance of the Lower
694 and Upper Cretaceous turbidites in the Central Pontides (Northern Turkey) related to the
695 opening of the Black Sea: *Tectonics* v. 38, p. 1050–1069,
696 <https://doi.org/10.1029/2018TC005119>.

697 Akdoğan, R., Okay, A.I., Sunal, G., Tari, G., Meinhold, G., and Kylander-Clark, A.R., 2017,
698 Provenance of a large Lower Cretaceous turbidite submarine fan complex on the active
699 Laurasian margin: Central Pontides, northern Turkey: *Journal of Asian Earth Sciences*, v.
700 134, p. 309–329, <https://doi.org/10.1016/j.jseaes.2016.11.028>.

701 Akdoğan, R., Hu, X., Okay, A.I., Topuz, G., and Xue, W., 2021, Provenance of the Paleozoic to
702 Mesozoic siliciclastic rocks of the Istanbul Zone constrains the timing of the Rheic Ocean

- 703 closure in the Eastern Mediterranean region: *Tectonics*, v. 40, e2021TC006824,
704 <https://doi.org/10.1029/2021TC006824>.
- 705 Allen, M.B., Morton, A.C., Fanning, C.M., Ismail-Zadeh, A.J. and Kroonenberg, S.B., 2006,
706 Zircon age constraints on sediment provenance in the Caspian region: *Journal of the*
707 *Geological Society, London*, v. 163, p. 647–655, <https://doi.org/10.1144/0016-764920-068>.
- 708 Altıner, D., Koçyiğit, A., Farinacci, A., Nicosia, U., and Conti, M.A., 1991, Jurassic, Lower
709 Cretaceous stratigraphy and paleogeographic evolution of the southern part of north-
710 western Anatolia: *Geologica Romana*, v. 28, p. 13–80.
- 711 Andersen, T., Elburg, M.A., and Magwaza, B.N., 2019, Sources of bias in detrital zircon
712 geochronology: Discordance, concealed lead loss and common lead correction: *Earth-*
713 *Science Reviews*, v. 197, 102899, <https://doi.org/10.1016/j.earscirev.2019.102899>.
- 714 Ardila, A.M.M., Paterson, S.R., Memeti, V., Parada, M.A., and Molina, P.G., 2019, Mantle
715 driven Cretaceous flare-ups in Cordilleran arcs: *Lithos*, v. 326, p. 19–27,
716 <https://doi.org/10.1016/j.lithos.2018.12.007>.
- 717 Avigad, D., Abbo, A., Gerdes, A., and Schmitt, A.K., 2022, Crustal evolution of Western Europe:
718 Constraints from detrital zircon U-Pb-Hf-O isotopes: *Gondwana Research*, v. 106, p. 379–
719 396, <https://doi.org/10.1016/j.gr.2022.02.006>.
- 720 Aysal, N., Ustaömer, T., Öngen, S., Keskin, M., Köksal, S., Peytcheva, I., and Fanning, M., 2012,
721 Origin of the Early-Middle Devonian magmatism in the Sakarya Zone, NW Turkey:
722 geochronology, geochemistry and isotope systematics: *Journal of Asian Earth Sciences*, v.
723 45, p. 201–222, <https://doi.org/10.1016/j.jseaes.2011.10.011>.

- 724 Aysal, N., Şahin, S.Y., Güngör, Y., Peytcheva, I., and Öngen, S., 2018, Middle Permian–Early
725 Triassic magmatism in the Western Pontides, NW Turkey: geodynamic significance for the
726 evolution of the Paleo-Tethys: *Journal of Asian Earth Sciences*, v. 164, p. 83–103,
727 <https://doi.org/10.1016/j.jseaes.2018.06.026>.
- 728 Babaoğlu, C., Topuz, G., Okay, A. I., Köksal, S., Wang, J. M., and Toksoy-Köksal, F., 2023,
729 Middle Permian basic and acidic volcanism in the Istanbul zone (NW Turkey): evidence for
730 post-Variscan extensional magmatism. *International Geology Review*, 1-18.
731 <https://doi.org/10.1080/00206814.2023.2188551>.
- 732 Balgord, E.A., Yonkee, W.A., Wells, M.L., Gentry, A., and Laskowski, A.K., 2021, Arc tempos,
733 tectonic styles, and sedimentation patterns during evolution of the North American
734 Cordillera: Constraints from the retroarc detrital zircon archive: *Earth-Science Reviews*, v.
735 216, 103557, <https://doi.org/10.1016/j.earscirev.2021.103557>.
- 736 Bozkurt, E., Holdsworth, B.K., and Koçyiğit, A., 1997. Implications of Jurassic chert identified
737 in the Tokat Complex, northern Turkey: *Geological Magazine*, v. 134, p. 91–97,
738 <https://doi.org/10.1017/S0016756897006419>.
- 739 Bozkurt, E., Winchester, J.A., and Satır, M., 2013, The Çele mafic complex: evidence for
740 Triassic collision between the Sakarya and İstanbul Zones, NW Turkey: *Tectonophysics*, v.
741 595, p. 198–214, <https://doi.org/10.1016/j.tecto.2012.11.005>.
- 742 Çapkınoğlu, Ş., and Bektaş, O., 1998, Karakaya Kompleksine ait Karasenir Formasyonu
743 (Amasya) içindeki kireçtaşı olistolitlerinden Erken Devoniyen konodontları: *Maden Teknik*
744 *Arama Enstitüsü Dergisi*, v. 120, p. 159–170.

- 745 Catlos, E.J., Huber, K., and Shin, T.A., 2013, Geochemistry and geochronology of meta-igneous
746 rocks from the Tokat Massif, north-central Turkey: implications for Tethyan
747 reconstructions: *International Journal of Earth Sciences*, v. 102, p. 2175–2198,
748 <https://doi.org/10.1007/s00531-013-0918-0>.
- 749 Çelik, Ö.F., Topuz, G., Billor, Z., and Özkan, M., 2019a, Middle Jurassic subduction-related
750 ophiolite fragment in Triassic accretionary complex (Mamu Dağı ophiolite, Northern
751 Turkey): *International Geology Review*, v. 61, p. 2021–2035,
752 <https://doi.org/10.1080/00206814.2019.1578109>.
- 753 Çelik, Ö.F., Özkan, M., Chelle-Michou, C., Sherlock, S., Marzoli, A., Ulianov, A., Altıntaş, I.E.,
754 and Topuz, G., 2019b, Blueschist facies overprint of late Triassic Tethyan oceanic crust in a
755 subduction–accretion complex in north-central Anatolia, Turkey: *Journal of the Geological*
756 *Society* v. 176, p. 945–957, <https://doi.org/10.1144/jgs2018-045>.
- 757 Chapman, J.B., Shields, J.E., Ducea, M.N., Paterson, S.R., Attia, S., and Ardill, K.E., 2021, The
758 causes of continental arc flare ups and drivers of episodic magmatic activity in Cordilleran
759 orogenic systems: *Lithos*, v. 398, 106307, <https://doi.org/10.1016/j.lithos.2021.106307>.
- 760 Cohen, K.M., Finney, S.C., Gibbard, P.L., and Fan, J.-X., 2013; updated, The ICS International
761 Chronostratigraphic Chart: *Episodes*, v. 36, p. 199–204,
762 <https://doi.org/10.18814/epiiugs/2013/v36i3/002>.
763 <http://www.stratigraphy.org/ICSchart/ChronostratChart2021-10.pdf>.
- 764 DeCelles, P.G., Ducea, M.N., Kapp, P., and Zandt, G., 2009, Cyclicality in Cordilleran orogenic
765 systems: *Nature Geoscience*, v. 2, p. 251–257, <https://doi.org/10.1038/ngeo469>.

- 766 Dickinson, W.R., 2008, Impact of differential zircon fertility of granitoid basement rocks in
767 North America on age populations of detrital zircons and implications for granite
768 petrogenesis: *Earth and Planetary Science Letters*, v. 275, p. 80–92,
769 <https://doi.org/10.1016/j.epsl.2008.08.003>.
- 770 Dokuz, A., 2011, A slab detachment and delamination model for the generation of Carboniferous
771 high-potassium I-type magmatism in the Eastern Pontides, NE Turkey: The Köse
772 composite pluton: *Gondwana Research*, v. 19, p. 926–944,
773 <https://doi.org/10.1016/j.gr.2010.09.006>.
- 774 Dokuz, A., Külekçi, E., Aydınçakır, E., Kandemir, R., Alçiçek, M.C., Pecha, M.E., and Sünnetçi,
775 K., 2017, Cordierite-bearing strongly peraluminous Cebre Rhyolite from the eastern
776 Sakarya zone, NE Turkey: Constraints on the Variscan orogeny: *Lithos*, v. 278, p. 285–302,
777 <https://doi.org/10.1016/j.lithos.2017.02.002>.
- 778 Dokuz, A., Gücer, M.A., Karşlı, O., and Yi, K., 2022, From Cadomian back-arc basin to Rheic
779 Ocean closure: the geochronological records of the Kurtoğlu Massif, eastern Sakarya Zone,
780 Turkey: *International Journal of Earth Sciences*, v. 111, p. 1333–1355,
781 <https://doi.org/10.1007/s00531-022-02183-4>.
- 782 Ducea, M.N., and Barton, M.D., 2007, Igniting flare-up events in Cordilleran arcs: *Geology*, v.
783 35, p. 1047–1050, <https://doi.org/10.1130/G23898A.1>.
- 784 Eyüboğlu, Y., Santosh, M., Bektas, O., and Chung, S.L., 2011, Late Triassic subduction-related
785 ultramafic–mafic magmatism in the Amasya region (eastern Pontides, N. Turkey):
786 Implications for the ophiolite conundrum in Eastern Mediterranean: *Journal of Asian Earth
787 Sciences*, v. 42, p. 234–257, <https://doi.org/10.1016/j.jseas.2011.01.007>.

- 788 Eyüboğlu, Y., Dudas, F.O., Chatterjee, N., Santosh, M., Billor, M.Z., and Yuva, S., 2018,
789 Petrology, geochronology and tectonic setting of early Triassic alkaline metagabbros from
790 the Eastern Pontide Orogenic Belt (NE Turkey): Implications for the geodynamic evolution
791 of Gondwana's early Mesozoic northern margin: *Tectonics*, v. 37, p. 3174–3206,
792 <https://doi.org/10.1029/2017TC004837>.
- 793 Franke, W., 2000, The mid-European segment of the Variscides: tectono-stratigraphic units,
794 terrane boundaries and plate tectonic evolution. /n: Franke, W., Haak, V., Oncken, O. and
795 Tanner, D. (Eds.) *Orogenic Processes: Quantification and Modelling in the Variscan Belt*.
796 Geological Society, London, Special Publications, v. 179, p. 35–62.
- 797 Genç, Ş.C., and Tüysüz, O., 2010, Tectonic setting of the Jurassic bimodal magmatism in the
798 Sakarya Zone (Central and Western Pontides), Northern Turkey: a geochemical and
799 isotopic approach: *Lithos*, v. 118, p. 95–111, <https://doi.org/10.1016/j.lithos.2010.03.017>.
- 800 Grimes, C.B., Wooden, J.L., Cheadle, M.J., and John, B.E., 2015, “Fingerprinting” tectono-
801 magmatic provenance using trace elements in igneous zircon: *Contributions to Mineralogy*
802 and *Petrology*, v. 170, p. 1–26, <https://doi.org/10.1007/s00410-015-1199-3>.
- 803 Hakyemez, H.Y., and Papak, I., compilers, 2002, Geological map of Turkey, Samsun, General
804 Directorate of Mineral Research and Exploration (M.T.A.), Ankara, scale 1:500,000, one
805 sheet.
- 806 Hoskin, P.W., and Schaltegger, U., 2003, The composition of zircon and igneous and
807 metamorphic petrogenesis: *Reviews in Mineralogy and Geochemistry*, v. 53, p. 27–62,
808 <https://doi.org/10.2113/0530027>.

- 809 Kandemir, R., and Yılmaz, C., 2009, Lithostratigraphy, facies, and deposition environment of the
810 lower Jurassic Ammonitico Rosso type sediments (ARTS) in the Gümüşhane area, NE
811 Turkey: implications for the opening of the northern branch of the Neo-Tethys Ocean:
812 *Journal of Asian Earth Sciences*, v. 34, p. 586–598,
813 <https://doi.org/10.1016/j.jseaes.2008.08.006>.
- 814 Karlı, O., Dokuz, A., and Kandemir, R., 2016, Subduction-related Late Carboniferous to Early
815 Permian magmatism in the Eastern Pontides, the Camlik and Casurluk plutons: insights
816 from geochemistry, whole-rock Sr–Nd and in situ zircon Lu–Hf isotopes, and U–Pb
817 geochronology: *Lithos*, v. 266, p. 98–114, <https://doi.org/10.1016/j.lithos.2016.10.007>.
- 818 Karlı, O., Şengün, F., Dokuz, A., Kandemir, R., Aydın, F., and Andersen, T., 2020, Silurian to
819 Early Devonian arc magmatism in the western Sakarya Zone (NW Turkey), with inference
820 to the closure of the Rheic ocean: *Lithos*, v. 370, 105641,
821 <https://doi.org/10.1016/j.lithos.2020.105641>.
- 822 Kaygusuz, A., Arslan, M., Siebel, W., Sipahi, F., and İlbeyli, N., 2012, Geochronological
823 evidence and tectonic significance of Carboniferous magmatism in the southwest Trabzon
824 area, eastern Pontides, Turkey: *International Geology Review*, v. 54, p. 1776–1800,
825 <https://doi.org/10.1080/00206814.2012.676371>.
- 826 Kaygusuz, A., Arslan, M., Sipahi, F., and Temizel, İ., 2016, U–Pb zircon chronology and
827 petrogenesis of Carboniferous plutons in the northern part of the Eastern Pontides, NE
828 Turkey: constraints for Paleozoic magmatism and geodynamic evolution: *Gondwana
829 Research*, v. 39, p. 327–346, <https://doi.org/10.1016/j.gr.2016.01.011>.

- 830 Kuznetsov, N.B., Belousova, E.A., Griffin, W.L., O'Reilly, S.Y., Romanyuk, T.V., and Rud'ko,
831 S.V., 2019, Pre-Mesozoic Crimea as a continuation of the Dobrogea platform: Insights
832 from detrital zircons in Upper Jurassic conglomerates, Mountainous Crimea: *International*
833 *Journal of Earth Sciences*, v. 108, p. 2407–2428, [https://doi.org/10.1007/s00531-019-](https://doi.org/10.1007/s00531-019-01770-2)
834 [01770-2](https://doi.org/10.1007/s00531-019-01770-2).
- 835 Laurent, O., Couzinié, S., Zeh, A., Vanderhaeghe, O., Moyen, J. F., Villaros, A., Gardien, V., and
836 Chelle-Michou, C., 2017, Protracted, coeval crust and mantle melting during Variscan late-
837 orogenic evolution: U–Pb dating in the eastern French Massif Central: *International Journal*
838 *of Earth Sciences*, v. 106, p. 421–451, <https://doi.org/10.1007/s00531-016-1434-9>.
- 839 Laurent, O., Moyen, J.F., Wotzlaw, J.F., Björnsen, J., and Bachmann, O., 2022, Early Earth
840 zircons formed in residual granitic melts produced by tonalite differentiation: *Geology*, v.
841 50, p. 437–441, <https://doi.org/10.1130/G49232.1>.
- 842 Liu, Z., Zhu, D.C., Wang, Q., Eyuboglu, Y., Zhao, Z.D., Liu, S.A., and Xu, L.J., 2018, Transition
843 from low-K to high-K calc-alkaline magmatism at approximately 84 Ma in the Eastern
844 Pontides (NE Turkey): Magmatic response to slab rollback of the Black Sea: *Journal of*
845 *Geophysical Research: Solid Earth*, v. 123(9), p. 7604–7628,
846 <https://doi.org/10.1029/2018JB016026>.
- 847 Liu, Z., Zhu, D.C., Wang, Q., Cawood, P.A., Ma, A.L., Eyüboğlu, Y., Wu, F-Y., and Zhao, Z.D.,
848 2022, Was there an exchange of detritus between the northern and southern Black Sea
849 terranes in the Mesozoic-early Cenozoic? *Gondwana Research*, v. 104, p. 154–171,
850 <https://doi.org/10.1016/j.gr.2021.06.011>.

- 851 Ludwig, K.R., 2003, User's manual for Isoplot 3.00: A geochronological toolkit for Microsoft
852 Excel: Berkeley, California, Berkeley Geochronology Center Special Publication 4, 74 p.
- 853 Malusà, M.G., Carter, A., Limoncelli, M., Villa, I.M., and Garzanti, E., 2013, Bias in detrital
854 zircon geochronology and thermochronometry. *Chemical Geology*, v. 359, p. 90–107,
855 <https://doi.org/10.1016/j.chemgeo.2013.09.016>.
- 856 Mayringer, F., Treloar, P.J., Gerdes, A., Finger, F., and Shengelia, D., 2011. New age data from
857 the Dzirula massif, Georgia: Implications for the evolution of the Caucasian Variscides:
858 *American Journal of Science*, v. 311, p. 404–441, <https://doi.org/10.2475/05.2011.02>.
- 859 Moazzen, M., Salimi, Z., Rolland, Y., Bröcker, M., and Hajialioghli, R., 2020, Protolith nature
860 and P–T evolution of Variscan metamorphic rocks from the Allahyarlu complex, NW Iran.
861 *Geological Magazine*, v. 157, p. 1853–1876. <https://doi.org/10.1017/S0016756820000102>.
- 862 Moecher, D.P., and Samson, S.D., 2006, Differential zircon fertility of source terranes and
863 natural bias in the detrital zircon record: Implications for sedimentary provenance analysis:
864 *Earth and Planetary Science Letters*, v. 247, p. 252–266,
865 <https://doi.org/10.1016/j.epsl.2006.04.035>.
- 866 Mueller, M.A., Licht, A., Campbell, C., Oçakoğlu, F., Taylor, M.H., Burch, L., Ugrai, T.,
867 Kurtoğlu, B., Coster, P.M.C., Métais, G., and Beard, K.C., 2019, Collision chronology
868 along the İzmir-Ankara-Erzincan suture zone: Insights from the Sarıcakaya Basin, western
869 Anatolia: *Tectonics*, v. 38, p. 3652–3674, <https://doi.org/10.1029/2019TC005683>.
- 870 Mueller, M.A., Licht, A., Campbell, C., Oçakoğlu, F., Akşit, G.G., Métais, G., Coster, P.M.C.,
871 Beard, K.C., and Taylor, M.H., 2022, Sedimentary provenance from the evolving forearc-
872 to-foreland Central Sakarya Basin, western Anatolia reveals multi-phase intercontinental

- 873 collision. *Geochemistry Geophysics Geosystems* 23, e2021GC010232,
874 <https://doi.org/10.1029/2021GC010232>
- 875 Nikishin, A.M., Romanyuk, T.V., Moskovskii, D.V., Kuznetsov, N.B., Kolesnikova, A.A.,
876 Dubenskii, A.S., Sheshukov, V.S., and Lyapunov, S.M., 2020, Upper Triassic sequences of
877 the Crimean Mountains: First results of U–Pb dating of detrital zircons: *Moscow University*
878 *Geology Bulletin*, v. 75, p. 220–236, <https://doi.org/10.3103/S0145875220030096>.
- 879 Nzegge, O.M., Satir, M., Siebel, W., and Taubald, H., 2006, Geochemical and isotopic
880 constraints on the genesis of the Late Paleozoic Deliktaş and Sivrikaya granites from the
881 Kastamonu granitoid belt (Central Pontides, Turkey): *Neues Jahrbuch für Mineralogie*
882 *Abhandlungen*, v. 183, p. 27–40, <https://doi.org/10.1127/0077-7757/2006/0057>.
- 883 Okay, A.I., and Leven, E-Ja., 1996. Stratigraphy and paleontology of the upper Paleozoic
884 sequences in the Pular (Bayburt) region, Eastern Pontides: *Turkish Journal of Earth*
885 *Sciences*, v. 5, p. 145–155.
- 886 Okay, A.I., and Monié, P., 1997, Early Mesozoic subduction in the Eastern Mediterranean:
887 evidence from Triassic eclogite in northwest Turkey: *Geology*, v. 25, p. 595–598,
888 [https://doi.org/10.1130/0091-7613\(1997\)025<0595:EMSITE>2.3.CO;2](https://doi.org/10.1130/0091-7613(1997)025<0595:EMSITE>2.3.CO;2).
- 889 Okay, A.I., and Göncüoğlu M.C., 2004, The Karakaya Complex: a review of data and concepts:
890 *Turkish Journal of Earth Sciences*, v. 13, p. 75–95.
- 891 Okay, A.I., and Nikishin, A.M., 2015, Tectonic evolution of the southern margin of Laurasia in
892 the Black Sea region: *International Geology Review*, v. 57, p. 1051–1076,
893 <https://doi.org/10.1080/00206814.2015.1010609>.

- 894 Okay, A.I., and Topuz, G., 2017, Variscan orogeny in the Black Sea region: International Journal
895 of Earth Sciences, v. 106, p. 569–592, <https://doi.org/10.1007/s00531-016-1395-z>.
- 896 Okay, A. I., Monod, O., and Monié, P., 2002, Triassic blueschists and eclogites from northwest
897 Turkey: vestiges of the Paleo-Tethyan subduction: *Lithos*, v. 64, p. 155–178,
898 [https://doi.org/10.1016/S0024-4937\(02\)00200-1](https://doi.org/10.1016/S0024-4937(02)00200-1).
- 899 Okay A.I., Satır, M., and Siebel W., 2006, Pre-Alpide orogenic events in the Eastern
900 Mediterranean region, in Gee, D.G., and Stephenson, R.A., eds., *European Lithosphere*
901 *Dynamics*, Geological Society of London Memoirs 32, pp. 389–405,
902 <https://doi.org/10.1144/GSL.MEM.2006.032.01.23>.
- 903 Okay, A.I., Bozkurt, E., Satır, M., Yiğitbaş, E., Crowley, Q.G., and Shang, C.K., 2008, Defining
904 the southern margin of Avalonia in the Pontides: geochronological data from the Late
905 Proterozoic and Ordovician granitoids from NW Turkey: *Tectonophysics*, v. 461, p. 252–
906 264, <https://doi.org/10.1016/j.tecto.2008.02.004>.
- 907 Okay, A.I., Sunal, G., Sherlock, S., Altıner, D., Tüysüz, O., Kylander-Clark, A.R., and Aygül,
908 M., 2013, Early Cretaceous sedimentation and orogeny on the active margin of Eurasia:
909 Southern Central Pontides, Turkey: *Tectonics*, v. 32, p. 1247–1271,
910 <https://doi.org/10.1002/tect.20077>.
- 911 Okay, A.I., Sunal, G., Sherlock, S., Kylander-Clark, A.R., and Özcan, E., 2020, İzmir-Ankara
912 Suture as a Triassic to Cretaceous Plate Boundary—Data from Central Anatolia: *Tectonics*,
913 v. 39, e2019TC005849, <https://doi.org/10.1029/2019TC005849>.

- 914 Özgül, N., 1984, Stratigraphy and tectonic evolution of the Central Taurides. In: Tekeli, O. and
915 Göncüoğlu, M.C. (Eds.) *Geology of the Taurus Belt*, pp. 77–90.
- 916 Özgül, N., and Kozlu, H., 2002, Kozan-Feke (Doğu Toroslar) yöresinin stratigrafisi ve yapısal
917 konumu ile ilgili bulgular: *Türkiye Petrol Jeologları Derneği Bülteni*, v. 14, p. 1–36.
- 918 Pastor-Galan, D., Spencer, C.J., Furukawa, T., and Tsujimori, T., 2021, Evidence for crustal
919 removal, tectonic erosion and flare-ups from the Japanese evolving forearc sediment
920 provenance: *Earth and Planetary Science Letters*, v. 564, 116893,
921 <https://doi.org/10.31223/X55P64>.
- 922 Paterson, S.R., and Ducea, M.N., 2015, Arc magmatic tempos: Gathering the evidence: *Elements*,
923 v. 11, p. 91–98, <https://doi.org/10.2113/gselements.11.2.91>.
- 924 Pickett, E.A., and Robertson, A.H.F., 1996, Formation of the Late Palaeozoic–Early Mesozoic
925 Karakaya Complex and related ophiolites in NW Turkey by Palaeotethyan subduction–
926 accretion: *Journal of the Geological Society*, v. 153, p. 995–1009,
927 <https://doi.org/10.1144/gsjgs.153.6.0995>.
- 928 Robertson, A.H.F., and Ustaömer, T., 2012, Testing alternative tectono-stratigraphic
929 interpretations of the late Palaeozoic– early Mesozoic Karakaya complex in NW Turkey:
930 Support for an accretionary origin related to northward subduction of Palaeotethys: *Turkish*
931 *Journal of Earth Sciences*, v. 21, p. 961–1007, <https://doi.org/10.3906/yer-1003-22>.
- 932 Robertson, A.H., Parlak, O., and Ustaömer, T., 2021, Late Palaeozoic extensional volcanism
933 along the northern margin of Gondwana in southern Turkey: implications for Palaeotethyan

- 934 development: *International Journal of Earth Sciences*, v. 110, p. 1961–1994.
935 <https://doi.org/10.1007/s00531-021-02051-7>
- 936 Rolland, Y., 2017, *Caucasus collisional history: Review of data from East Anatolia to West Iran:*
937 *Gondwana Research*, v. 49, p. 130–146, <https://doi.org/10.1016/j.gr.2017.05.005>.
- 938 Rolland, Y., Hässig, M., Bosch, D., Meijers, M. J. M., Sosson, M., Bruguier, O., Adamia, Sh.,
939 and Sadradze, N., 2016, A review of the plate convergence history of the East Anatolia-
940 Transcaucasus region during the Variscan: Insights from the Georgian basement and its
941 connection to the Eastern Pontides: *Journal of Geodynamics*, v. 96, p. 131–145.
942 <http://dx.doi.org/10.1016/j.jog.2016.03.003>.
- 943 Rojay, B., and Göncüoğlu, M.C., 1997, Tectonic setting of some pre-Liassic low-grade
944 metamorphics in northern Anatolia: *Yerbilimleri*, v. 19, p. 109–118.
- 945 Rossetti, F., Monié, P., Nasrabady, M., Theye, T., Lucci, F., & Saadat, M. (2017). Early
946 Carboniferous subduction-zone metamorphism preserved within the Palaeo-Tethyan Rasht
947 ophiolites (western Alborz, Iran): *Journal of the Geological Society [London]*, v. 174, p.
948 741–758. <https://doi.org/10.1144/jgs2016-130>.
- 949 Rubatto, D., 2002, Zircon trace element geochemistry: partitioning with garnet and the link
950 between U–Pb ages and metamorphism: *Chemical Geology*, v. 184, p. 123–138,
951 [https://doi.org/10.1016/S0009-2541\(01\)00355-2](https://doi.org/10.1016/S0009-2541(01)00355-2).
- 952 Sayit, K., and Göncüoğlu, M.C., 2009, Geochemistry of mafic rocks of the Karakaya complex,
953 Turkey: evidence for plume-involvement in the Palaeotethyan extensional regime during

- 954 the Middle and Late Triassic: *International Journal of Earth Sciences*, v. 98, p. 367–385,
955 <https://doi.org/10.1007/s00531-007-0251-6>.
- 956 Şen, C., 2007, Jurassic volcanism in the Eastern Pontides: is it rift related or subduction related?
957 *Turkish Journal of Earth Sciences* 16, 523–539.
- 958 Şengör, A.M.C., Lom, N., Sunal, G., Zabcı, C., and Sancar, T., 2019, The Phanerozoic
959 palaeotectonics of Turkey. Part I: an inventory: *Mediterranean Geoscience Reviews*, 1, 91–
960 161, <https://doi.org/10.1007/s42990-019-00007-3>.
- 961 Şengün, F., Koralay, O.E., and Kristoffersen, M., 2020, Zircon U-Pb age and Hf isotopic
962 composition of the Carboniferous Gönen granitoid in the western Sakarya Zone of Turkey:
963 *Turkish Journal of Earth Sciences*, v. 29, p. 617–628, <https://doi.org/10.3906/yer-1910-7>.
- 964 Shellnutt, J.G., Lee, T.Y., Brookfield, M.E., and Chung, S.L., 2014, Correlation between
965 magmatism of the Ladakh Batholith and plate convergence rates during the India–Eurasia
966 collision: *Gondwana Research*, v. 26, p. 1051–1059,
967 <https://doi.org/10.1016/j.gr.2013.09.006>.
- 968 Stampfli, G.M., and Borel, G.D., 2002, A plate tectonic model for the Paleozoic and Mesozoic
969 constrained by dynamic plate boundaries and restored synthetic oceanic isochrones: *Earth
970 Planetary Science Letters*, v. 196, p. 17–33, [https://doi.org/10.1016/S0012-821X\(01\)00588-
971 X](https://doi.org/10.1016/S0012-821X(01)00588-X).
- 972 Tekin, U.K., Göncüoğlu, M.C., and Turhan, N., 2002, First evidence of Late Carnian radiolarians
973 from the Izmir–Ankara suture complex, central Sakarya, Turkey: implications for the

- 974 opening age of the Izmir–Ankara branch of Neo-Tethys: *Geobios*, v. 35, p. 127–135,
975 [https://doi.org/10.1016/S0016-6995\(02\)00015-3](https://doi.org/10.1016/S0016-6995(02)00015-3).
- 976 Topuz, G., Altherr, R., Satır, M., Schwarz, W.H., 2004a, Low-grade metamorphic rocks from the
977 Pulur complex, NE Turkey: implications for the pre-Liassic evolution of the Eastern
978 Pontides: *International Journal of Earth Sciences*, v. 93, p. 72–91,
979 <https://doi.org/10.1007/s00531-003-0372-5>.
- 980 Topuz, G., Altherr, R., Kalt, A., Satır, M., Werner, O., Schwarz, W.H., 2004b, Aluminous
981 granulites from the Pulur complex, NE Turkey: a case of partial melting, efficient melt
982 extraction and crystallization: *Lithos*, v. 72, p. 183–207,
983 <https://doi.org/10.1016/j.lithos.2003.10.002>.
- 984 Topuz, G., Altherr, R., Siebel, W., Schwarz, W.H., Zack, T., Hasözbeğ, A., Barth, M., Satır, M.,
985 and Şen, C., 2010, Carboniferous high-potassium I-type granitoid magmatism in the
986 Eastern Pontides: The Gümüşhane pluton (NE Turkey): *Lithos*, v. 116, p. 92–110,
987 <https://doi.org/10.1016/j.lithos.2010.01.003>.
- 988 Topuz, G., Göçmengil, G., Rolland, Y., Çelik, Ö.F., Zack, T., and Schmitt, A.K., 2013, Jurassic
989 accretionary complex and ophiolite from northeast Turkey: No evidence for the Cimmerian
990 continental ribbon: *Geology*, v. 45, p. 255–258, <https://doi.org/10.1130/G33577.1>.
- 991 Topuz, G., Okay, A.I., Altherr, R., Schwarz, W.H., Sunal, G., and Altınkaynak, L., 2014, Triassic
992 warm subduction in northeast Turkey: Evidence from the Ağvanis metamorphic rocks:
993 *Island Arc*, v. 23, p. 181–205, <https://doi.org/10.1111/iar.12068>.
- 994 Topuz, G., Okay, A.I., Schwarz, W.H., Sunal, G., Altherr, R., and Kylander-Clark, A.R., 2018, A
995 Middle Permian ophiolite fragment in Late Triassic greenschist-to blueschist-facies rocks in

- 996 NW Turkey: An earlier pulse of suprasubduction-zone ophiolite formation in the Tethyan
997 belt: *Lithos*, v. 300, p. 121–135, <https://doi.org/10.1016/j.lithos.2017.12.005>.
- 998 Topuz, G., Candan, O., Okay, A. I., von Quadt, A., Othman, M., Zack, T., and Wang, J., 2020,
999 Silurian anorogenic basic and acidic magmatism in Northwest Turkey: Implications for the
1000 opening of the Paleo-Tethys: *Lithos*, v. 356, 105302,
1001 <https://doi.org/10.1016/j.lithos.2019.105302>.
- 1002 Topuz, G., Altherr, R., Candan, O., Wang, J-M., Okay, A.I., Wu, F-Y., Ergen, A., Zack, T.,
1003 Siebel, W., Shang, C.K., Schwarz, W.H., Meyer, H-P., and Satır, M., 2023, Carboniferous
1004 mafic-ultramafic intrusions in the Eastern Pontides (Pulur Complex): Implications for the
1005 source of coeval voluminous granites: *Lithos*, v. 436, 106946,
1006 <https://doi.org/10.1016/j.lithos.2022.106946>.
- 1007 Ustaömer, P.A., Ustaömer, T., and Robertson, A.H.F., 2012, Ion probe U-Pb dating of the Central
1008 Sakarya Basement: a peri-Gondwana terrane intruded by Late Lower Carboniferous
1009 subduction/collision-related granitic rocks: *Turkish Journal of Earth Sciences*, v. 21, p.
1010 905–932, <https://doi.org/10.3906/yer-1103-1>.
- 1011 Ustaömer, T., Robertson, A.H.F., Ustaömer, P.A., Gerdes, A., and Peytcheva, I., 2013,
1012 Constraints on Variscan and Cimmerian magmatism and metamorphism in the Pontides
1013 (Yusufeli–Artvin area), NE Turkey from U–Pb dating and granite geochemistry, *in*
1014 Robertson, A.H.F., Parlak, O., and Ünlügenç, U.C., eds, *Geological Development of*
1015 *Anatolia and the Easternmost Mediterranean Region*: Geological Society, London, Special
1016 Publication 372, p. 49–74, <https://doi.org/10.1144/SP372.13>.

- 1017 Ustaömer, T., Ustaömer, P.A., Robertson, A.H., and Gerdes, A., 2016, Implications of U–Pb and
1018 Lu–Hf isotopic analysis of detrital zircons for the depositional age, provenance and tectonic
1019 setting of the Permian–Triassic Palaeotethyan Karakaya Complex, NW Turkey:
1020 International Journal of Earth Sciences, v. 105, p. 7–38, [https://doi.org/10.1007/s00531-](https://doi.org/10.1007/s00531-015-1225-8)
1021 015-1225-8.
- 1022 Vermeesch, P., 2004, How many grains are needed for a provenance study?: Earth and Planetary
1023 Science Letters, v. 224, p. 441–451, <https://doi.org/10.1016/j.epsl.2004.05.037>.
- 1024 Vincent, S.J., Morton, A.C., Hyden, F., and Fanning, M., 2013. Insights from petrography,
1025 mineralogy and U-Pb zircon geochronology into the provenance and reservoir potential of
1026 Cenozoic siliciclastic depositional systems supplying the northern margin of the Eastern
1027 Black Sea: Marine and Petroleum Geology, v. 45, p. 331–348,
1028 <https://doi.org/10.1016/j.marpetgeo.2013.04.002>.
- 1029 Vincent, S.J., Guo, L., Flecker, R., BouDagher-Fadel, M.K., Ellam, R.M., and Kandemir, R.,
1030 2018, Age constraints on intra-formational unconformities in Upper Jurassic-Lower
1031 Cretaceous carbonates in northeast Turkey; geodynamic and hydrocarbon implications:
1032 Marine and Petroleum Geology, v. 91, p. 639–657,
1033 <https://doi.org/10.1016/j.marpetgeo.2018.01.011>.
- 1034 van Hinsbergen, D.J., Torsvik, T.H., Schmid, S.M., Mañenco, L.C., Maffione, M., Vissers, R.L.,
1035 Gürer, D., and Spakman, W., 2020, Orogenic architecture of the Mediterranean region and
1036 kinematic reconstruction of its tectonic evolution since the Triassic: Gondwana Research,
1037 v. 81, p. 79–229, <https://doi.org/10.1016/j.gr.2019.07.009>.

- 1038 von Raumer, J.F., Bussy, F., Schaltegger, U., Schulz, B., and Stampfli, G.M., 2013, Pre-
1039 Mesozoic Alpine basements—their place in the European Paleozoic framework: GSA
1040 Bulletin, v. 125, p. 89–108, <https://doi.org/10.1130/B30654.1>.
- 1041 Vanderhaeghe, O., Laurent, O., Gardien, V., Moyen, J. F., Gébelin, A., Chelle-Michou, C., ... and
1042 Bellanger, M., 2020, Flow of partially molten crust controlling construction, growth and
1043 collapse of the Variscan orogenic belt: the geologic record of the French Massif Central:
1044 BSGF - Earth Sciences Bulletin, v. 191, 25. <https://doi.org/10.1051/bsgf/2020013>.
- 1045 Wan, B., Chu, Y., Chen, L., Liang, X., Zhang, Z., Ao, S., and Talebian, M., 2021, Paleo-Tethys
1046 subduction induced slab-drag opening the Neo-Tethys: Evidence from an Iranian segment
1047 of Gondwana. Earth-Science Reviews, v. 221, p. 103788.
1048 <https://doi.org/10.1016/j.earscirev.2021.103788>
- 1049 Winchester, J.A., the PACE TMR Network Team (contract ERBFMRXCT97-0136), 2002,
1050 Palaeozoic amalgamation of Central Europe: new results from recent geological and
1051 geophysical investigations: Tectonophysics, v. 360, p. 5–21, [https://doi.org/10.1016/S0040-](https://doi.org/10.1016/S0040-1951(02)00344-X)
1052 [1951\(02\)00344-X](https://doi.org/10.1016/S0040-1951(02)00344-X).
- 1053 Yakymchuk, C., Kirkland, C.L., and Clark, C., 2018, Th/U ratios in metamorphic zircon: Journal
1054 of Metamorphic Geology, v. 36, p. 715–737, <https://doi.org/10.1111/jmg.12307>.
- 1055 Yılmaz, A., and Yılmaz, H., 2004, Geology and structural evolution of the Tokat Massif (eastern
1056 Pontides, Turkey): Turkish Journal of Earth Sciences, v. 13, p. 231–246.
- 1057 Yılmaz, Y., Serdar, H.S., Genc, C., Yigitbas, E., Gürer, Ö.F., Elmas, A., Yıldırım, M., Bozcu, M.,
1058 and Gürpinar, O., 1997, The geology and evolution of the Tokat Massif, south-central

1059 Pontides, Turkey: *International Geology Review*, v. 39, p. 365–382,

1060 <https://doi.org/10.1080/00206819709465278>.

1061 Zhang, X., Chung, S.L., Lai, Y.M., Ghani, A.A., Murtadha, S., Lee, H.Y., and Hsu, C.C., 2019, A

1062 6000-km-long Neo-Tethyan arc system with coherent magmatic flare-ups and lulls in South

1063 Asia: *Geology*, v. 47, p. 573–576, <https://doi.org/10.1130/G46172.1>.

1064 **FIGURE CAPTIONS**

1065 **Figure 1.** Simplified tectonic map of Europe and neighboring areas, showing main Phanerozoic

1066 sutures (modified after Topuz et al., 2020, and the references therein). Also are shown the

1067 drainage basins of the rivers Rhone, Evros, Nestos and Strymon.

1068 **Figure 2.** Distribution of the pre-Jurassic basement outcrops in northern Turkey (modified after

1069 Okay and Nikishin, 2015). IAES Izmir-Ankara-Erzincan suture; IPS Intra-Pontide suture;

1070 ITS Inner Tauride suture.

1071 **Figure 3.** Columnar section showing main pre-Jurassic basement units of the Sakarya Zone and

1072 its Jurassic-Cretaceous stratigraphy (modified after Topuz et al., 2020).

1073 **Figure 4.** Geological map of the Tokat Massif and the locations of the samples studied (modified

1074 after Hakyemez and Papak, 2002).

1075 **Figure 5.** U-Pb age distribution pattern of the detrital zircons from Middle Permian and Lower

1076 Jurassic sandstones from the Tokat Massif. Time scale is after Cohen et al. (2013, updated).

1077 **Figure 6. a** $^{206}\text{Pb}/^{238}\text{U}$ zircon ages (Ma) versus initial $\epsilon\text{Hf}(t)$ values of the detrital zircons from

1078 Lower Jurassic and Middle Permian sandstones from the Tokat Massif. **b** $^{206}\text{Pb}/^{238}\text{U}$ zircon

1079 ages (Ma) versus initial $\epsilon\text{Hf}(t)$ values of the Phanerozoic detrital zircons. In addition, the

1080 initial ϵHf values of zircons (dark blue lines; Karlı et al., 2016, 2020; Liu et al., 2018;
 1081 Şengün et al., 2020; Topuz et al., 2020) and initial ϵNd values of whole rocks (green bars;
 1082 Nzegge et al., 2006; Topuz et al., 2010; Dokuz, 2011; Aysal et al., 2012; Sunal, 2012;
 1083 Kaygusuz et al., 2012, 2016; Karlı et al., 2016) are shown.

1084 **Figure 7.** Compositional variation of the dated detrital zircon grains in (a) Nb/Yb versus U/Yb
 1085 after Grimes et al (2015), and (b) Hf versus Ti after Laurent et al. (2022).

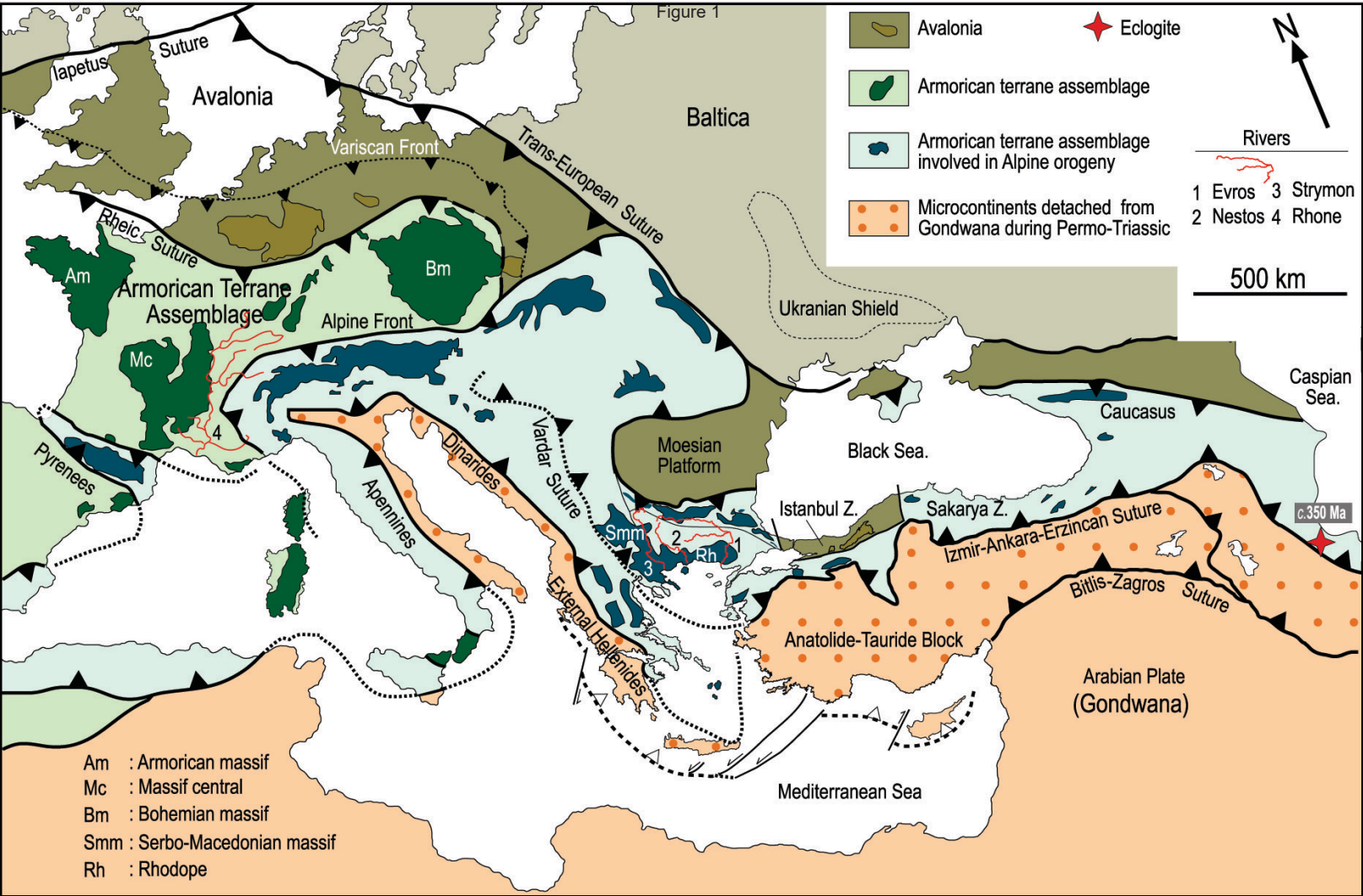
1086 **Figure 8.** U-Pb detrital zircon age histograms with probability density curves. Binwidth is set to
 1087 10 Ma. **a-b** This study, **c-d** the Late Triassic accretionary complexes in the western part of
 1088 the Sakarya Zone (data from Ustaömer et al., 2016), **e** the Upper Cretaceous sandstones
 1089 from the Sakarya Basin (data from Mueller et al. (2022), and **f** the Upper Cretaceous
 1090 sandstones from Samsun (data from Liu et al. 2022).

1091 **Figure 9.** Possible drivers of the Paleozoic and early Mesozoic magmatic flare-ups in the Sakarya
 1092 Zone. **a** Paleogeographic reconstruction for Late Carboniferous-Early Permian (modified
 1093 after Stampfli et al., 2013), **b** 212–199 Ma magmatic flare-up probably caused by slab
 1094 rollback and detachment after the accretion of an oceanic plateau or a seamount chain (Sc).
 1095 Bc Baltica, Av Avalonia, Iz Istanbul Zone, Sz Sakarya Zone. **c** 250–230 Ma magmatic
 1096 flare-up probably resulted from the northward subduction of the Paleo-Tethys (Pt) under
 1097 Laurasia. **d** 325–310 Ma magmatic flare-up possibly originated by the removal of
 1098 lowermost lithosphere after the accretion of Armorica (Arm) to Laurussia. **e** 400–380 Ma
 1099 magmatic flare-up is probably related to the southward subduction of the Rheic ocean
 1100 beneath the Sakarya Zone. **f** 440–420 Ma Silurian magmatic flare-up is ascribed to rift-
 1101 related magmatism leading to the detachment of Armorica from the northern margin of
 1102 Gondwana.

1103 **Figure 10.** U-Pb detrital zircon age histograms with probability density curves from the adjacent
1104 and distant Armorican terranes. **a** Middle-Upper? Jurassic sandstone from Greater
1105 Caucasus (data from Allen et al., 2006), **b** placer sand samples from the rivers Strymon,
1106 Nestos and Evros in the Balkans (data from Abbo et al., 2020), and **c** sand samples from the
1107 Rhone river delta (data from Avigad et al. 2022).

1108 **Supplemental Material** [Analytical Techniques, Figure S1. Comparative columnar sections of
1109 the Anatolide-Tauride Block and the Sakarya Zone, Figure S2. Field pictures, Figure S3. Thin
1110 section micrographs showing microtextural features of the studied sandstone samples, Figure S4.
1111 CL images of dated zircon grains, Figure S5. REE patterns of the dated zircon grains, Figure S6.
1112 Variation of U/Th, U/Yb and Nb/Yb ratios of the dated detrital zircon grains with age. Figure S7.
1113 U-Pb detrital zircon age histograms and probability density curves for literature data. Table S1
1114 Coordinates of the dated samples, Tables S2-S3 U-Pb and Hf metadata. Table S4 U-Pb-Th
1115 isotopic data and trace element compositions of zircons; Table S5 Hf isotopic data of zircons]
1116 Please visit <https://doi.org/10.1130/XXXX> to access the supplemental material, and contact
1117 editing@geosociety.org with any questions.

Figure 1





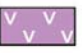





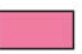

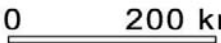


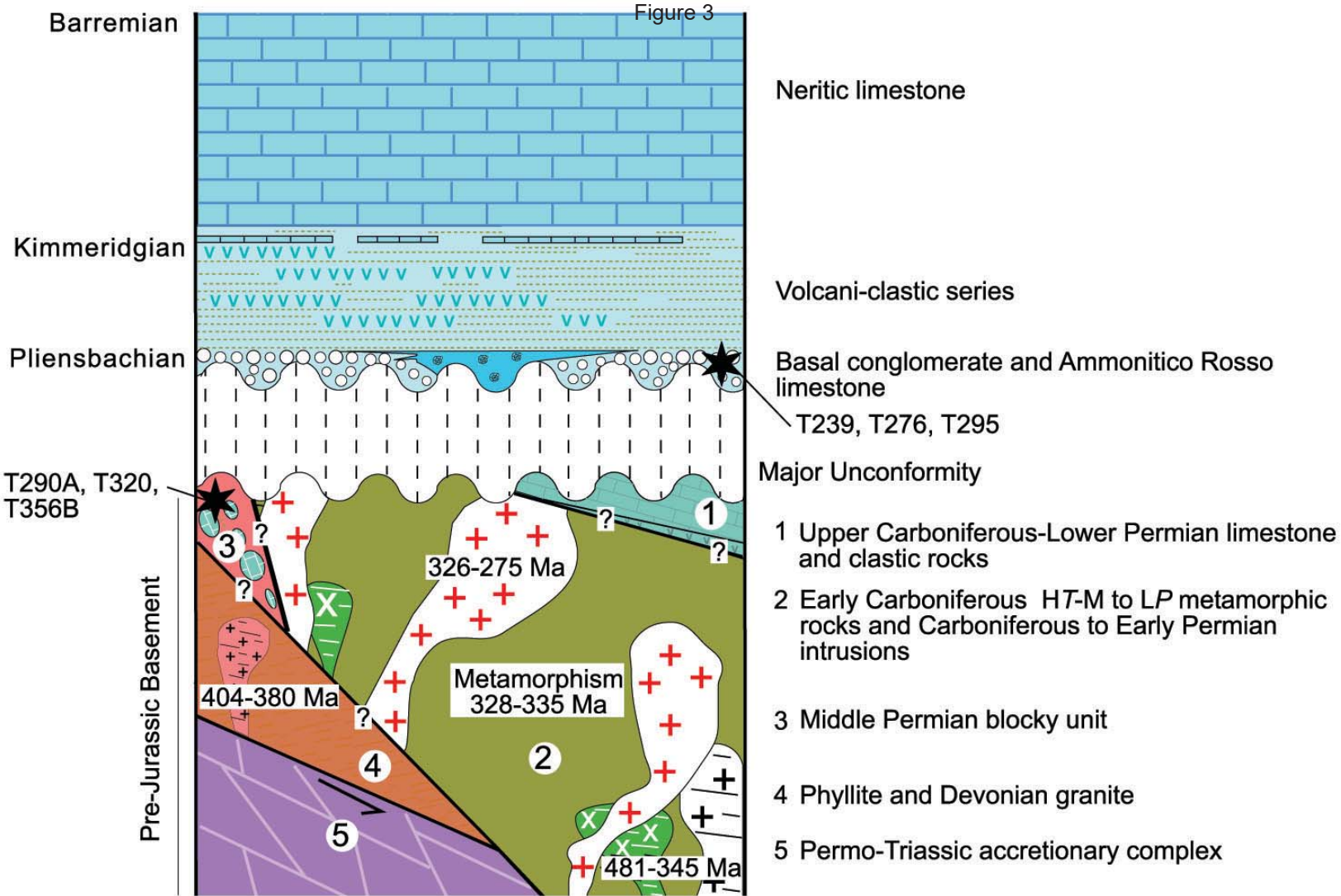
- | | | | | | |
|--|---|---|--|---|---------------------------------------|
|  | Inferred Triassic magmatic arc |  | Early Carboniferous high-grade metamorphic rocks with Alpine overprint |  | Post-Triassic rocks |
|  | Permo-Triassic low-grade metamorphic rocks |  | Carboniferous acidic to basic intrusions |  | Early to Late Carboniferous eclogites |
|  | Middle Permian blocky unit |  | Early Carboniferous high-grade metamorphic rocks |  | 0 200 km |
|  | Upper Carboniferous-Lower Permian sedimentary rocks |  | Early to Middle Devonian granites and low-grade metamorphic rocks | | |

Figure 3



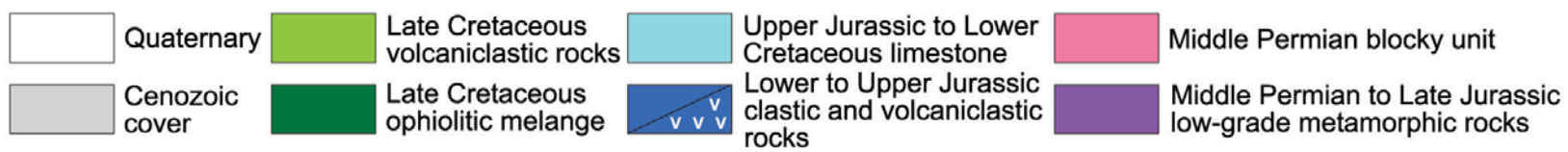
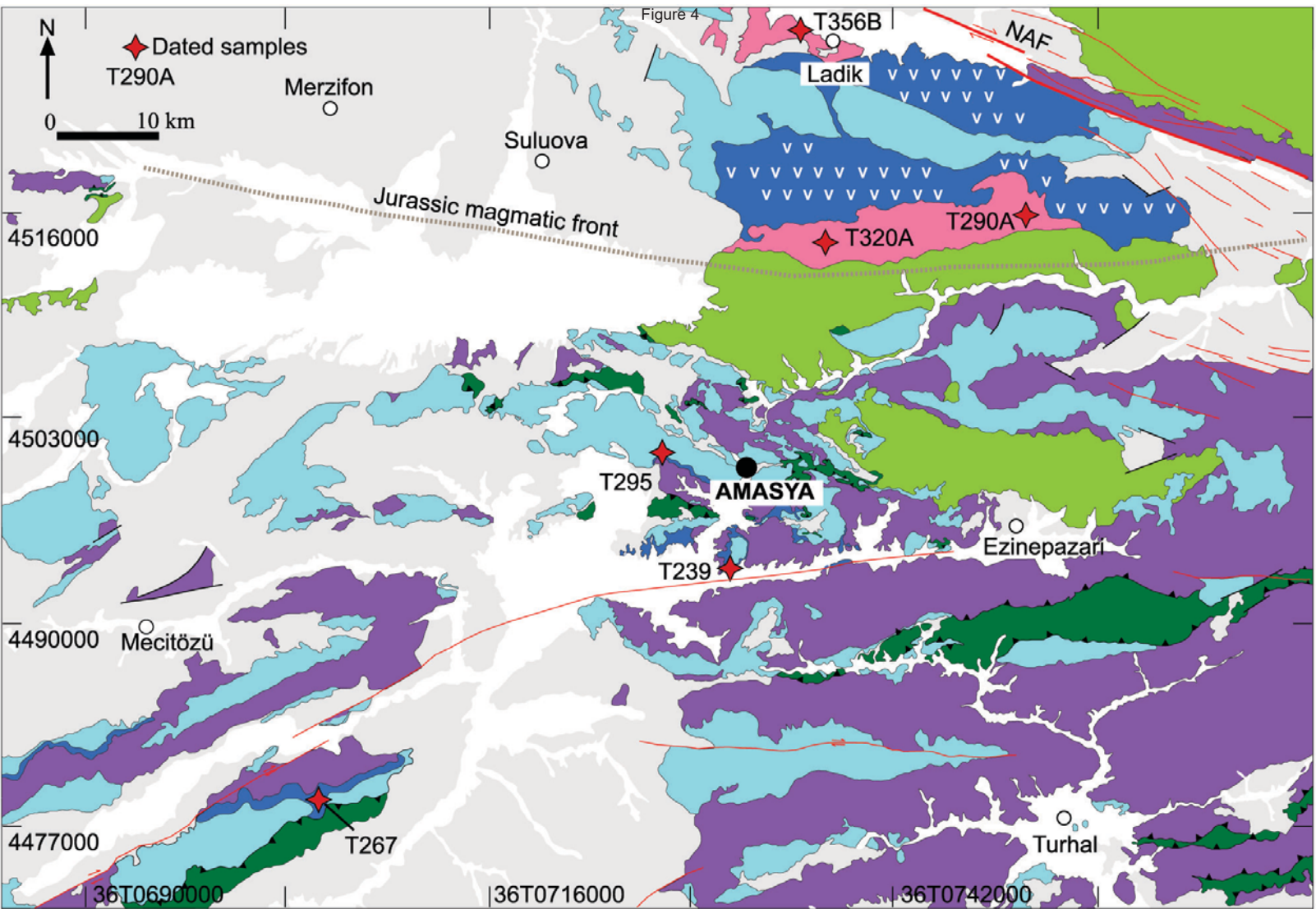


Figure 5

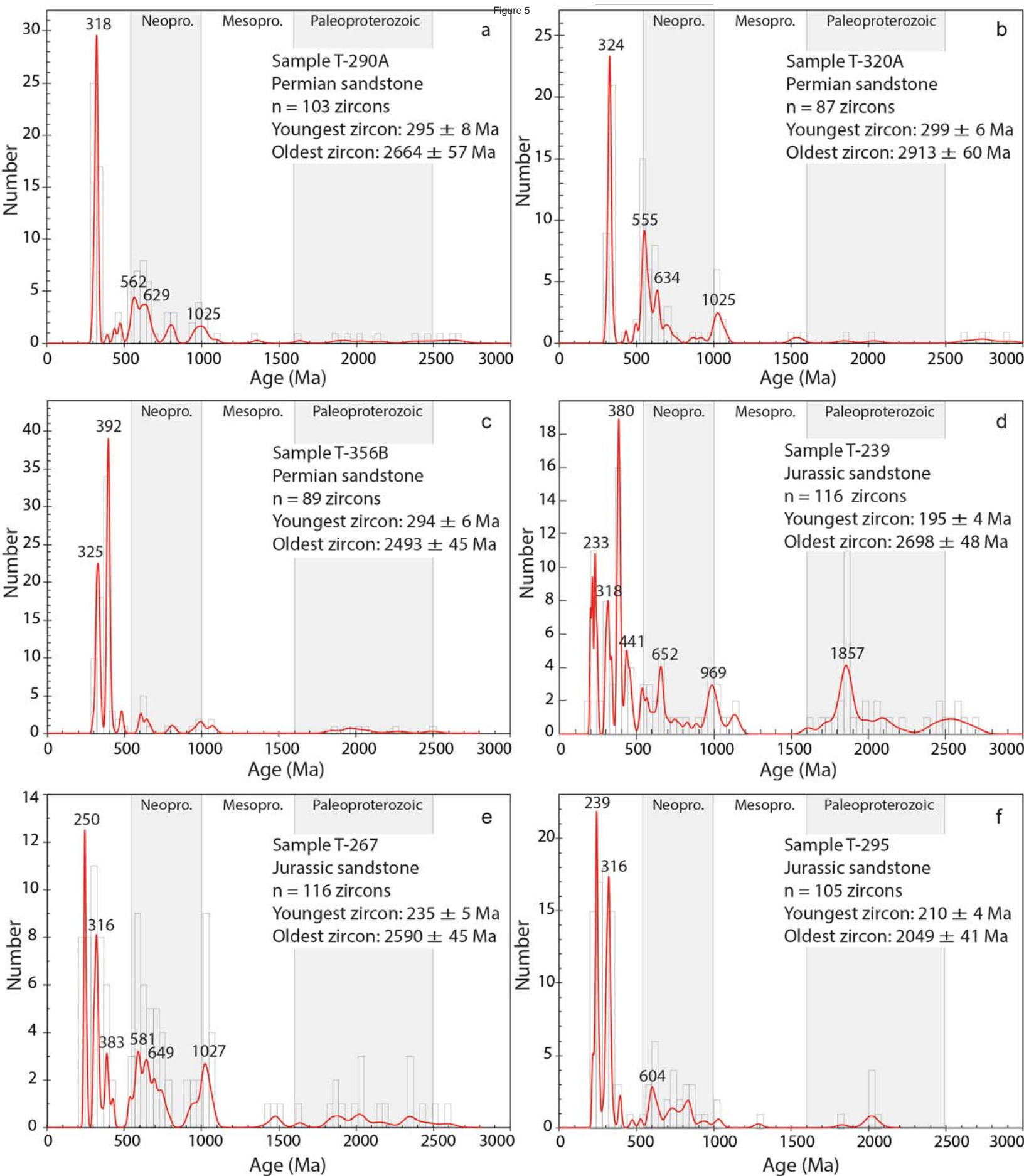


Figure 6

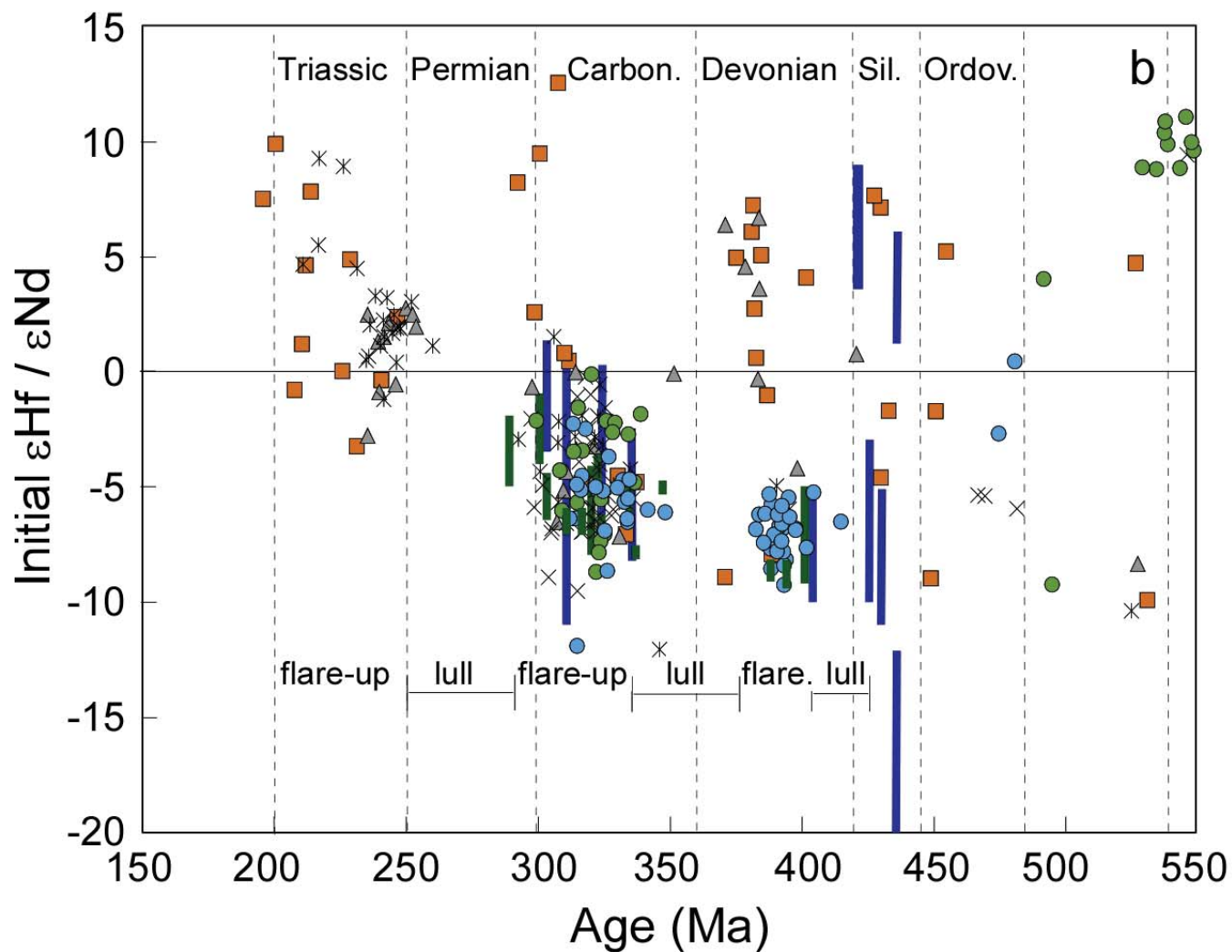
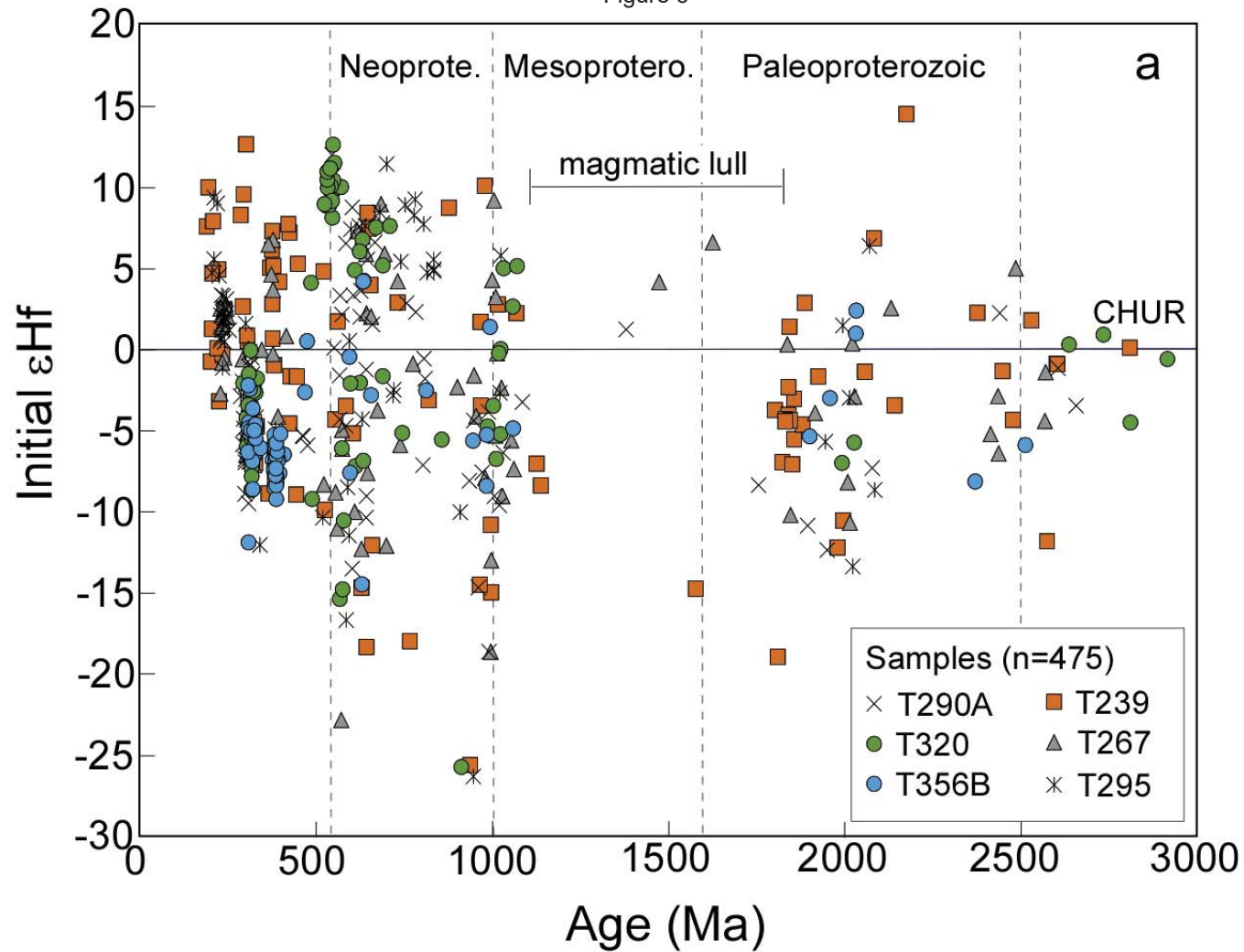


Figure 7

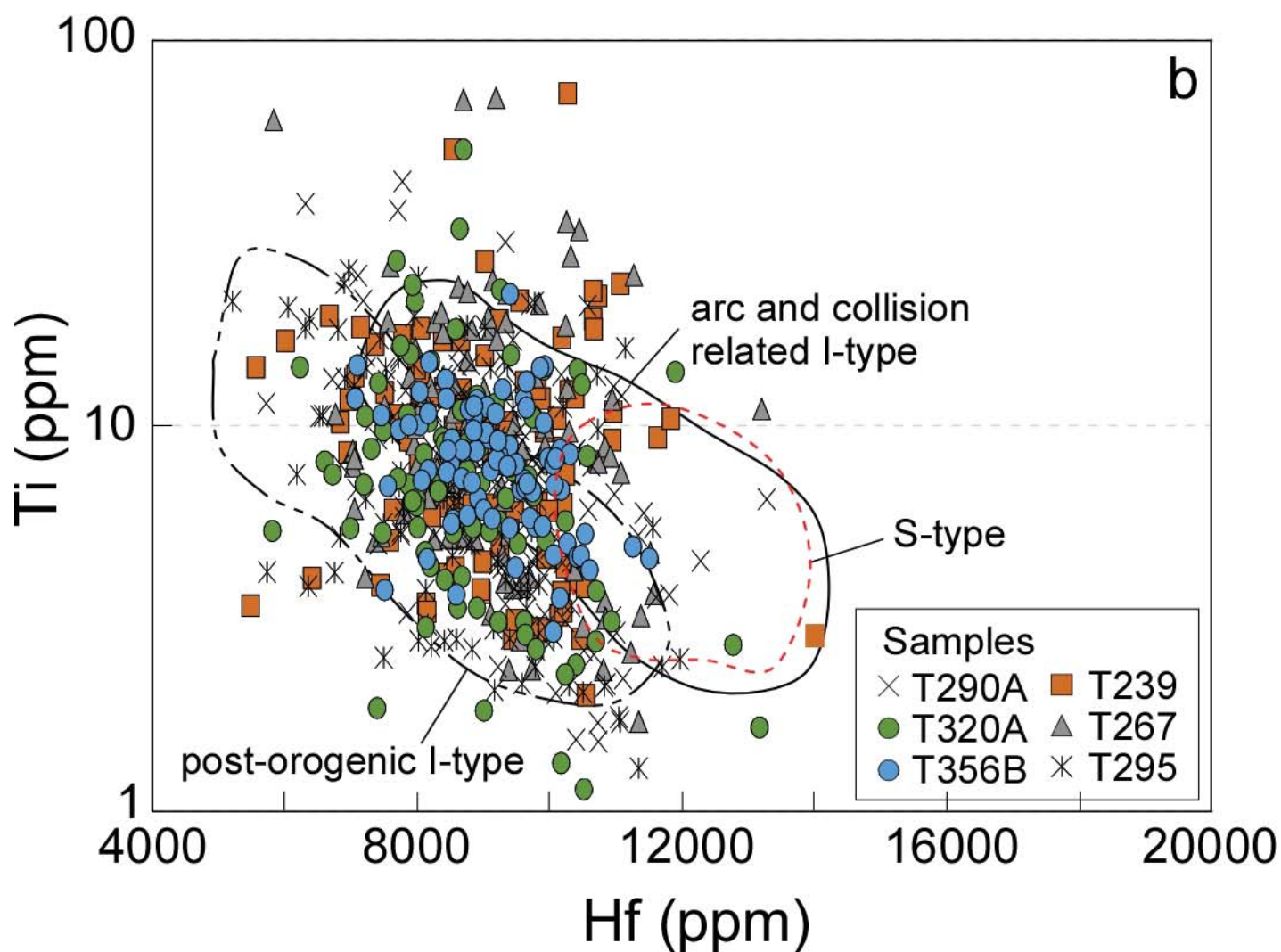
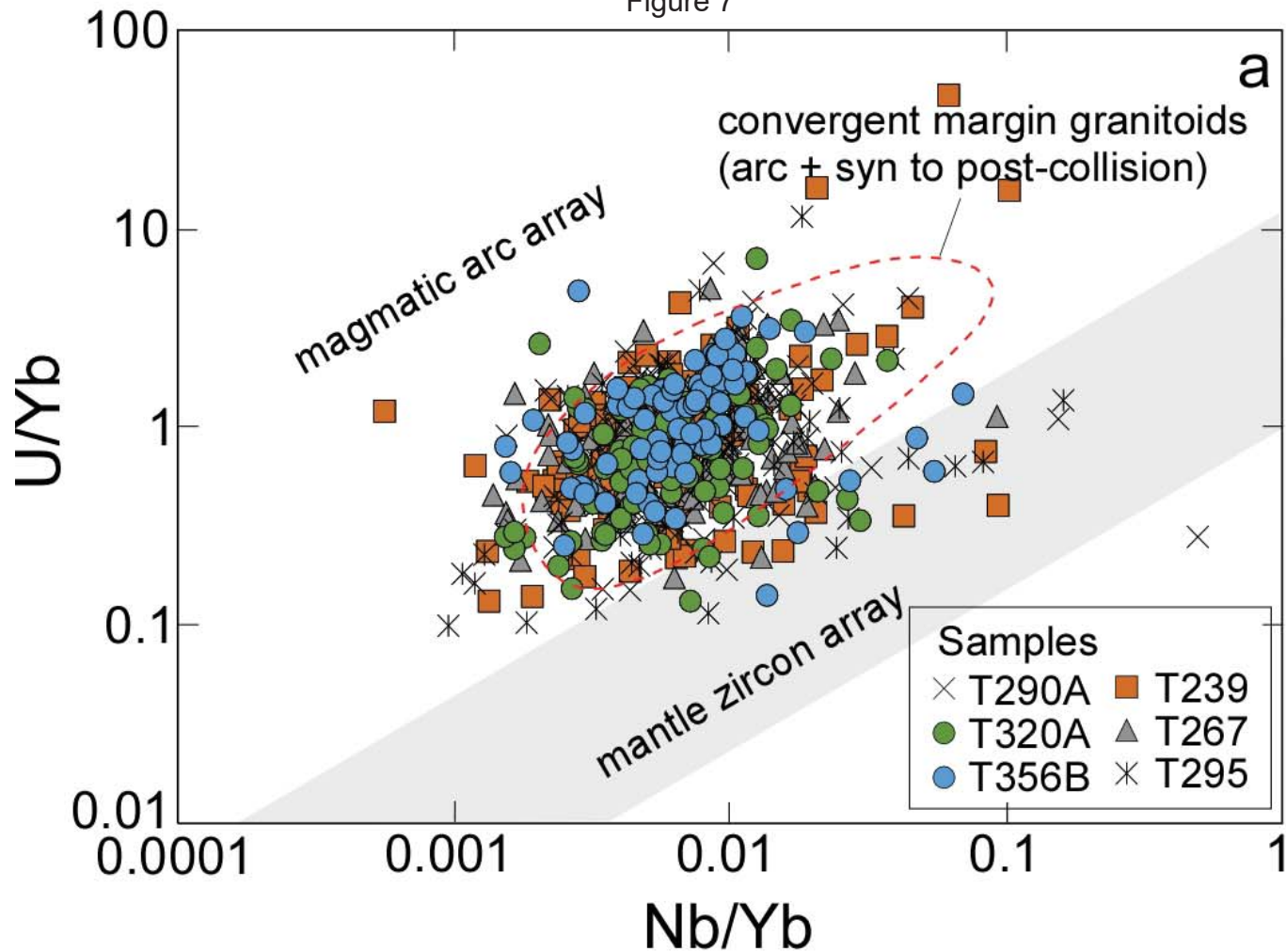
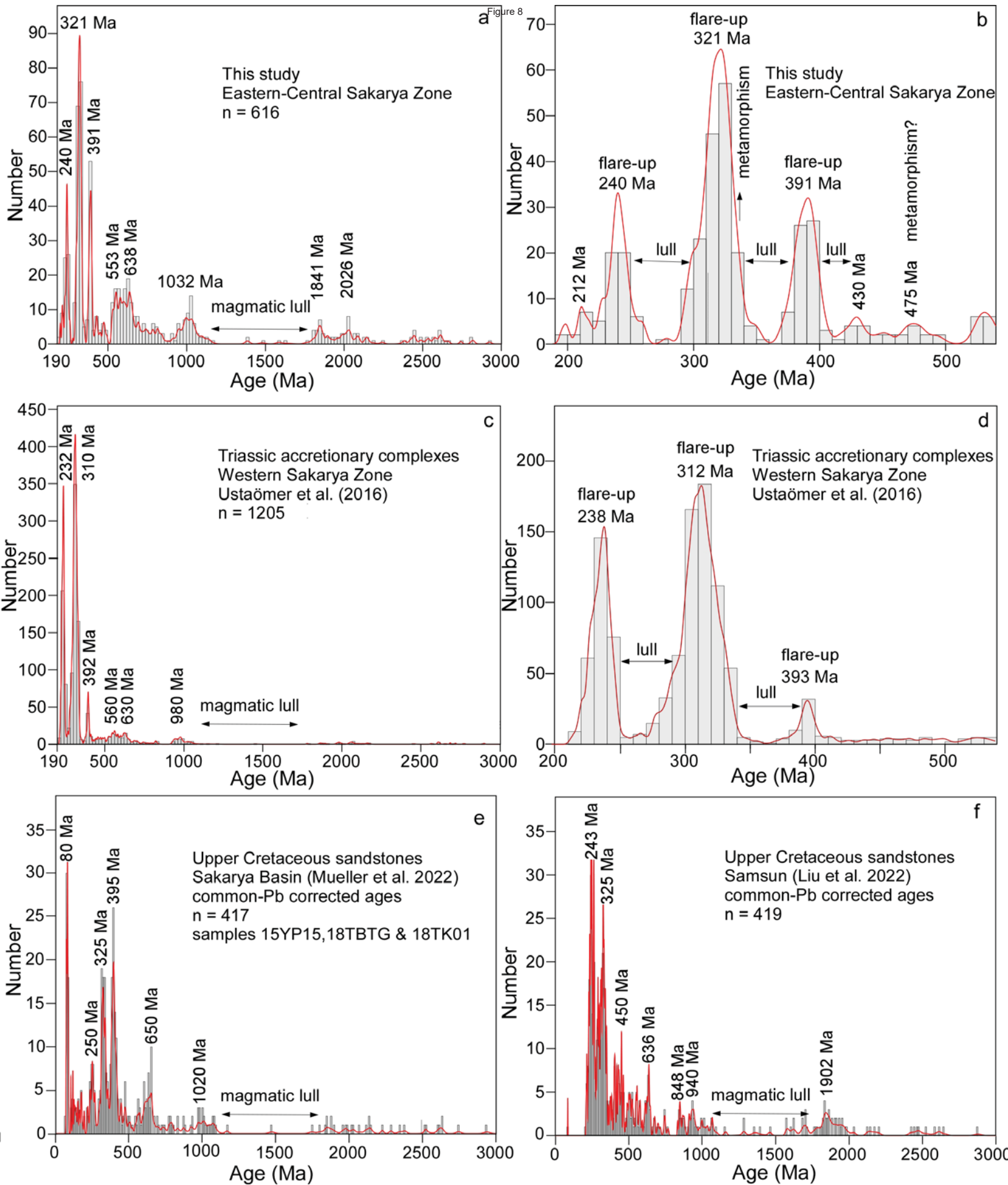
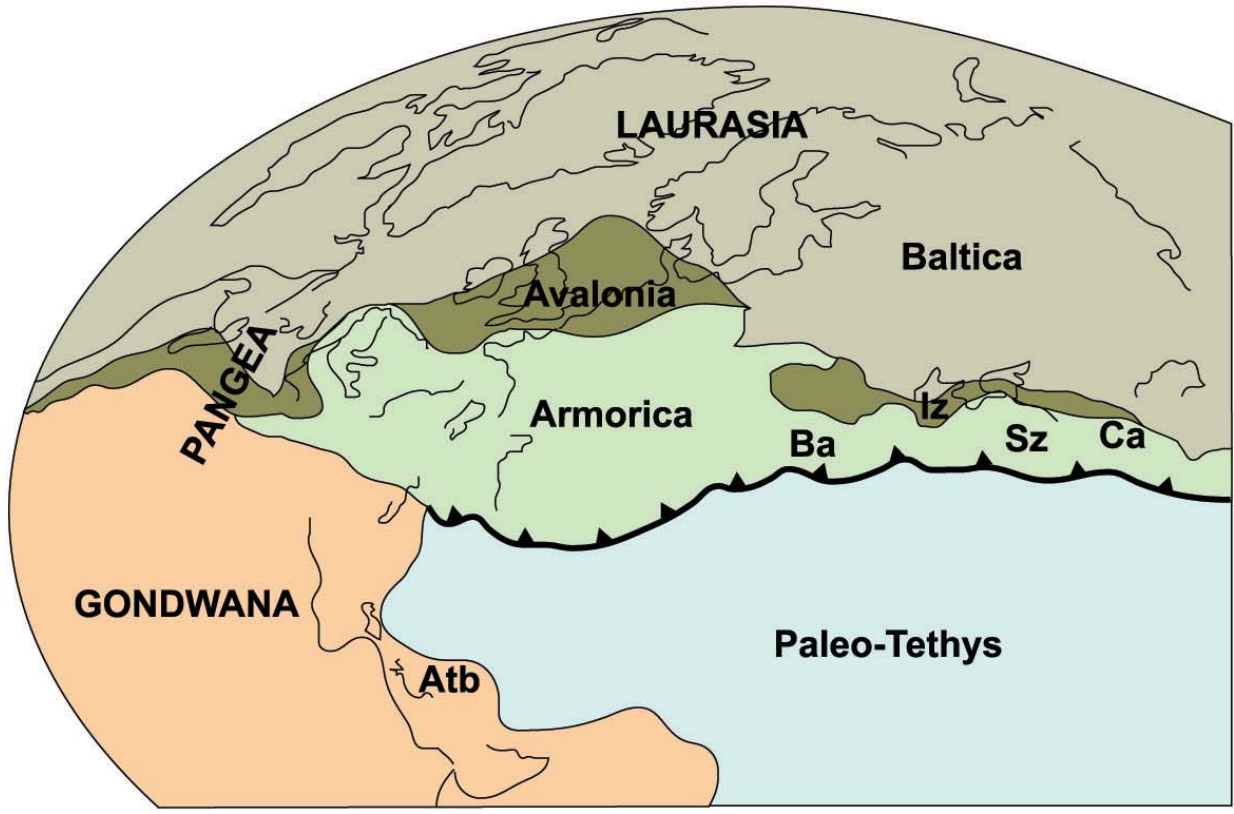


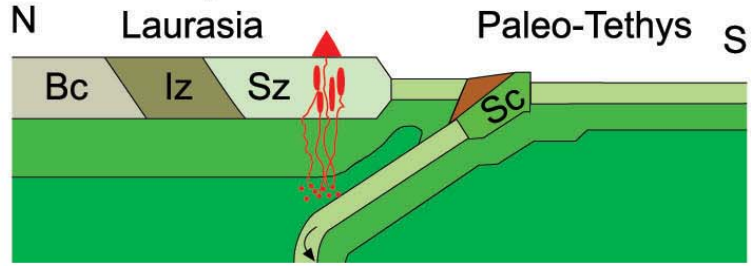
Figure 8



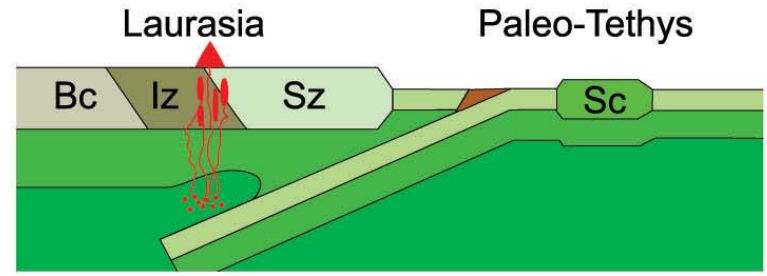
a Late Carboniferous-Early Permian



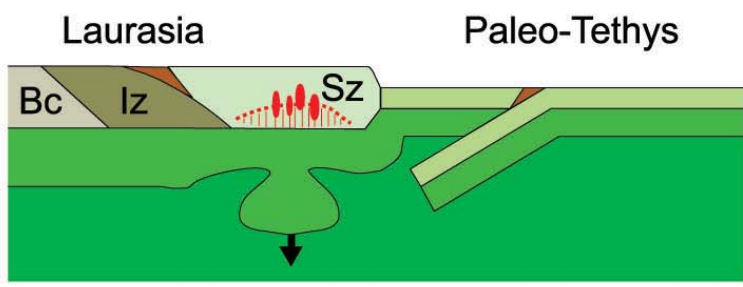
b 215-198 Ma (latest Triassic-earliest Jurassic)



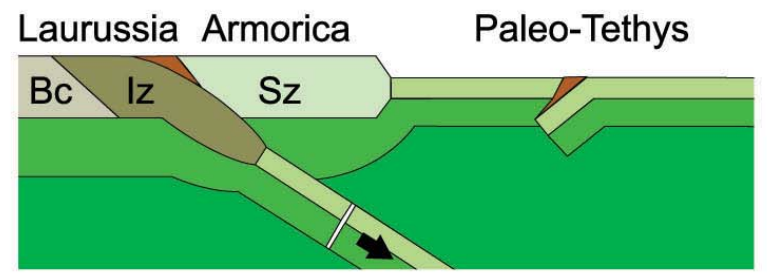
c 250-230 Ma (Triassic)



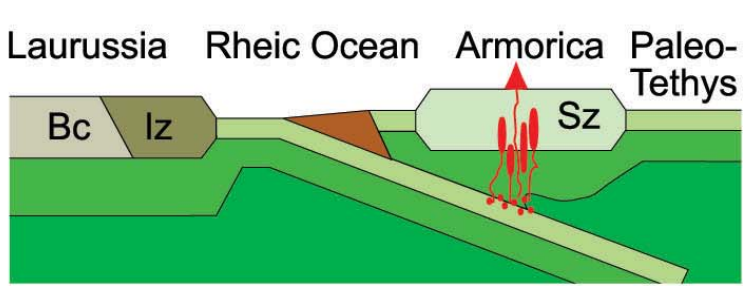
d 326-310 Ma (Late Carboniferous)



e ca.345 Ma (Early Carboniferous)



f 400-380 Ma (Middle Devonian)



g 460-430 Ma (Late Ordovician - Silurian)

